GEOLOGY

Mafic slab melt contributions to Proterozoic massif-type anorthosites

Duncan S. Keller[1]*, Cin-Ty A. Lee[1], William H. Peck[2], Brian D. Monteleone[3], Céline Martin[4], Jeffrey D. Vervoort[5], Louise Bolge[6]

Massif-type anorthosites, enormous and enigmatic plagioclase-rich cumulate intrusions emplaced into Earth's crust, formed in large numbers only between 1 and 2 billion years ago. Conflicting hypotheses for massif-type anorthosite formation, including melting of upwelling mantle, lower crustal melting, and arc magmatism above subduction zones, have stymied consensus on what parental magmas crystallized the anorthosites and why the rocks are temporally restricted. Using B, O, Nd, and Sr isotope analyses, bulk chemistry, and petrogenetic modeling, we demonstrate that the magmas parental to the Marcy and Morin anorthosites, classic examples from North America's Grenville orogen, require large input from mafic melts derived from slab-top altered oceanic crust. The anorthosites also record B isotopic signatures corresponding to other slab lithologies such as subducted abyssal serpentinite. We propose that anorthosite massifs formed underneath convergent continental margins wherein a subducted or subducting slab melted extensively and link massif-type anorthosite formation to Earth's thermal and tectonic evolution.

INTRODUCTION

Anorthosites are intrusive igneous rocks composed of ≥90% plagioclase feldspar that represent accumulated crystals concentrated from a crystallizing magma (*1*). On the modern Earth, where mafic magmatism occurs in oceanic spreading centers, above subducting slabs, and at intraplate hotspots, anorthosites form only as minor lenses, layers, or intrusions closely associated with their parental magmas (*1*, *2*). In contrast, an enigmatic style of anorthosite magmatism operated between 2.6 and 0.5 billion years ago (Ga). Only during this period did massif-type anorthosites, composite intrusions of plagioclase cumulates separated from their parental magma chambers and intruded into the continental crust, form worldwide. Between 1.8 and 0.9 Ga, during the assembly and persistence of the supercontinents Nuna and Rodinia, numerous massifs, including the largest known, were generated (Fig. 1). The largest massifs reach up to at least 42,000 km^2 in preserved extent and several kilometers in thickness (*3*), making them comparable to the texturally similar composite granitoid batholiths generated at modern convergent margins. The spatiotemporal patterns of anorthosite occurrence on Earth hint at fundamental changes in Earth's geodynamic and magmatic styles through time, but why massif-type anorthosites are restricted in time remains debated (*2*, *4*–*6*). Factors such as interplays between mantle temperatures and lithospheric strengthening (*4*), slower plate velocities (*5*), and effects from long-lived supercontinents and high mantle heat flow during the Proterozoic (*2*, *6*) have each been proposed as mechanisms favorable to the generation of the long-lived, voluminous mafic magmas parental to massif-type anorthosites.

Some key aspects of massif-type anorthosite genesis are well-constrained. Their primary mineralogy of intermediate-composition plagioclase (~$An_{30–70}$) with or without pyroxenes, olivine, and oxides, and little to no primary amphibole points to crystallization from mafic parental magmas with relatively low water activities (*1*, *4*, *7*, *8*). Restricted ranges of plagioclase composition at the massif scale (e.g., ~$An_{47±8}$ for the Marcy and Morin) suggest compositional buffering of the magmatic system, perhaps through recharge of long-lived parental magma chambers (*9*). The anorthosite bodies were emplaced into the continental crust, apparently in multiple pulses, as evidenced by the cross-cutting generations of anorthosite cumulates that can be observed in outcrop in many massifs (e.g., Fig. 2A). Emplacement of some massifs is well-constrained to mid- to upper-crustal depths (*1*, *7*, *10*). However, barometric constraints such as from high-Al pyroxene megacrysts formed at ~9 to 13 kbar that were entrained by ascending anorthositic mushes (Fig. 2, B and C) (*7*, *11*) suggest that plagioclase crystallization was a multistage process that happened, at least in part, at the base of the continental crust. These observations, as well as the observation that there is apparently insufficient preserved fossil mafic magma in or around the massifs to be complementary to the anorthosite cumulates, have led to the hypothesis that the anorthosites formed from ascending crystal-rich batches derived from a deeper system (*1*). Numerical modeling of these systems shows that buoyant rise of thick plagioclase cumulate mush piles could transport the anorthosites upward through the crust (*12*).

Despite these constraints on massif-type anorthosite formation, debate continues regarding the origins of the parental magmas and the tectonic setting(s) in which they were generated. Some studies argue for mafic parental magmas derived mostly from mantle sources [e.g., (*2*, *8*, *9*, *13*)], while other studies argue for mostly crustal sources [e.g., (*7*, *14*, *15*)]. Both divergent and convergent tectonic settings have been inferred to produce the massifs' parental magmas [see reviews in (*1*, *2*)], but most hypotheses invoke mantle melting through upwelling asthenosphere as the heat and/or melt source for anorthosite generation [e.g., (*16*)].

Recent geochronological studies have shown that some massif-type anorthosites were formed over time intervals of up to ~120 million years (*9*, *13*, *17*). These are unusually long time intervals for magmatism associated with plumes or divergent settings but are

[1]Department of Earth, Environmental and Planetary Sciences, Rice University, Houston, TX 77005, USA. [2]Department of Earth and Environmental Geosciences, Colgate University, Hamilton, NY 13346, USA. [3]Department of Geology and Geophysics, Woods Hole Oceanographic Institution, Woods Hole, MA 02543, USA. [4]Department of Earth and Planetary Sciences, American Museum of Natural History, New York, NY 10024, USA. [5]School of the Environment, Washington State University, Pullman, WA 99164, USA. [6]Lamont-Doherty Earth Observatory, Columbia University, Palisades, NY 10964, USA.
*Corresponding author. Email: dsk7@rice.edu

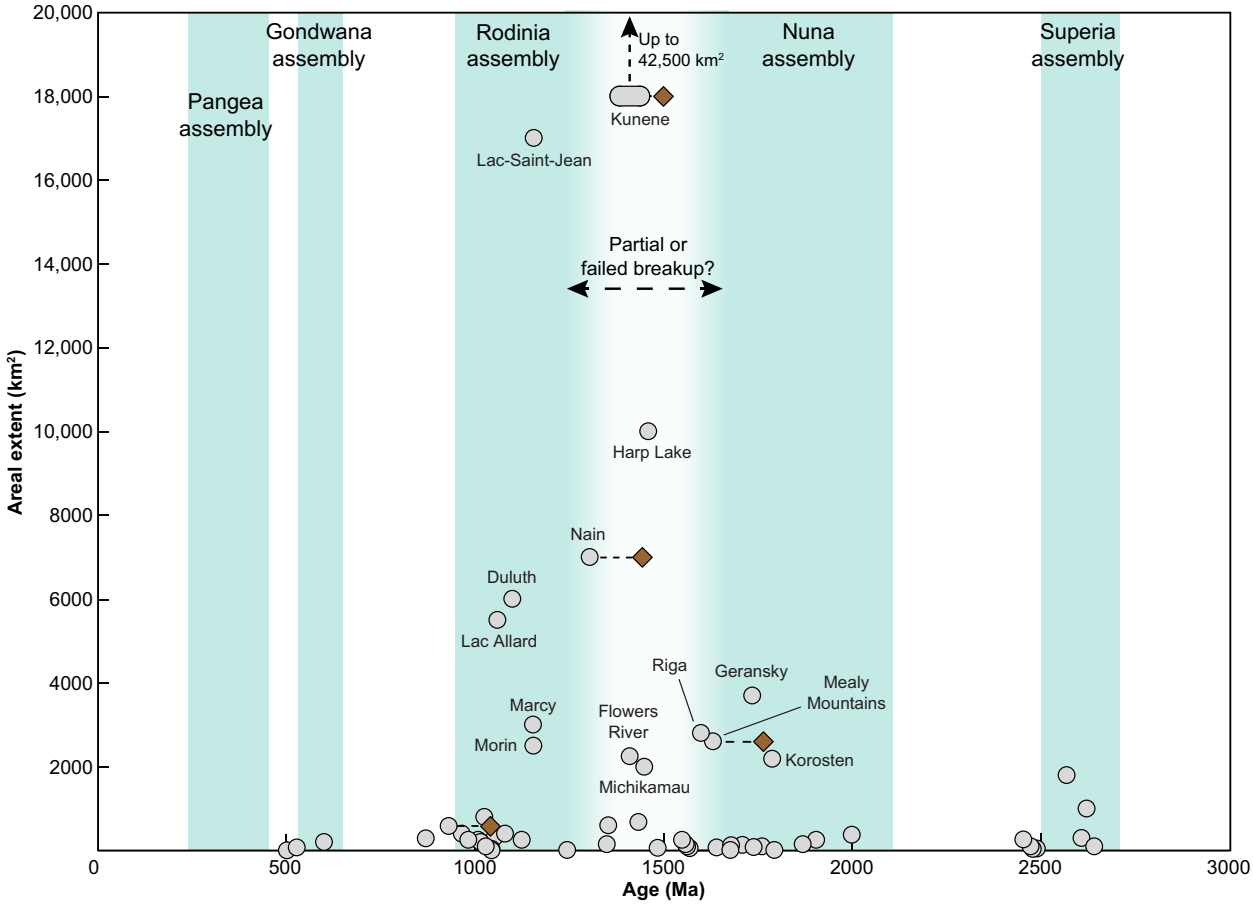

Fig. 1. Temporal distribution and size of massif-type anorthosites worldwide. Gray symbols represent the ages of anorthosite in the massifs; age uncertainties are not shown but are, in most cases, smaller than the symbol. Brown diamonds represent the ages of pyroxene megacrysts that have been dated and are connected to their host massif by a dotted line. Massif sizes and ages are from (*3*, *9*, *13*, *128*). Periods of supercontinent assembly are from (*129*). See (*6*) for discussion of failed or partial breakup of Nuna.

similar to geochronologic constraints for convergent settings. These findings have inspired the hypothesis that massif-type anorthosites are the products of long-lived magmatic systems underneath continental volcanic arcs (*9*, *13*). Phanerozoic continental arcs do not generate massif-type anorthosites, so if a convergent margin hypothesis is correct, then the profound implication is that Proterozoic continental arcs must have operated differently from those of the Phanerozoic (Fig. 1).

Here, we combine geochemical and petrological approaches to study the magmas parental to the Marcy and Morin anorthosites of the North American Grenville Province and test hypotheses of the massifs' formation. Because a convergent margin setting has been the focus of several recent studies of other massifs, we pair analyses of B and O stable isotopes, which are sensitive to subduction-related processes, with analyses of Nd and Sr radiogenic isotopes, which are sensitive to source reservoir age. Boron and O stable isotope analyses are particularly useful for detecting input from low-temperature altered oceanic crust (LTAOC; the pillow basalts and sheeted dikes in the upper kilometer of the oceanic crust altered by seawater at ≤400°C). Assimilation of LTAOC by the Marcy and Morin parental magmas has been hypothesized (*18*) but has not been tested using B isotopes. The combination of a major element stable isotope system (O) that accounts for a large fraction of the rock's mass with a trace element stable isotope system (B) that is highly sensitive to source lithology offers complementary information on magma sources. We integrate the B, O, Nd, and Sr isotope data with numerical modeling of magma crystallization and bulk rock chemistry to constrain the origins and evolution of the magmatic systems that produced the anorthosites.

RESULTS

Geologic background and samples

The Marcy and Morin massifs have well-documented geological histories and crop out within the Southern Grenville Province of eastern North America (fig. S1). Both massifs have emplacement ages of ~1155 million years ago (Ma) and comprise anorthosite, plagioclase-rich mafic rocks (e.g., leucogabbro and leuconorite), volumetrically minor gabbros and oxide-rich gabbros, and rare ultramafic lenses. Following their emplacement into the crust, both massifs were metamorphosed during the Ottawan phase of the Grenville Orogeny at ~1050 Ma (*19*–*21*). As indicated by rock textures and mineralogy, metamorphism was largely dry and isochemical, and in many rocks, original igneous features such as intercumulus relationships and exsolution textures are evident (Fig. 2, D and E). The consistency of anorthosite oxygen isotopic compositions at the massif scale further

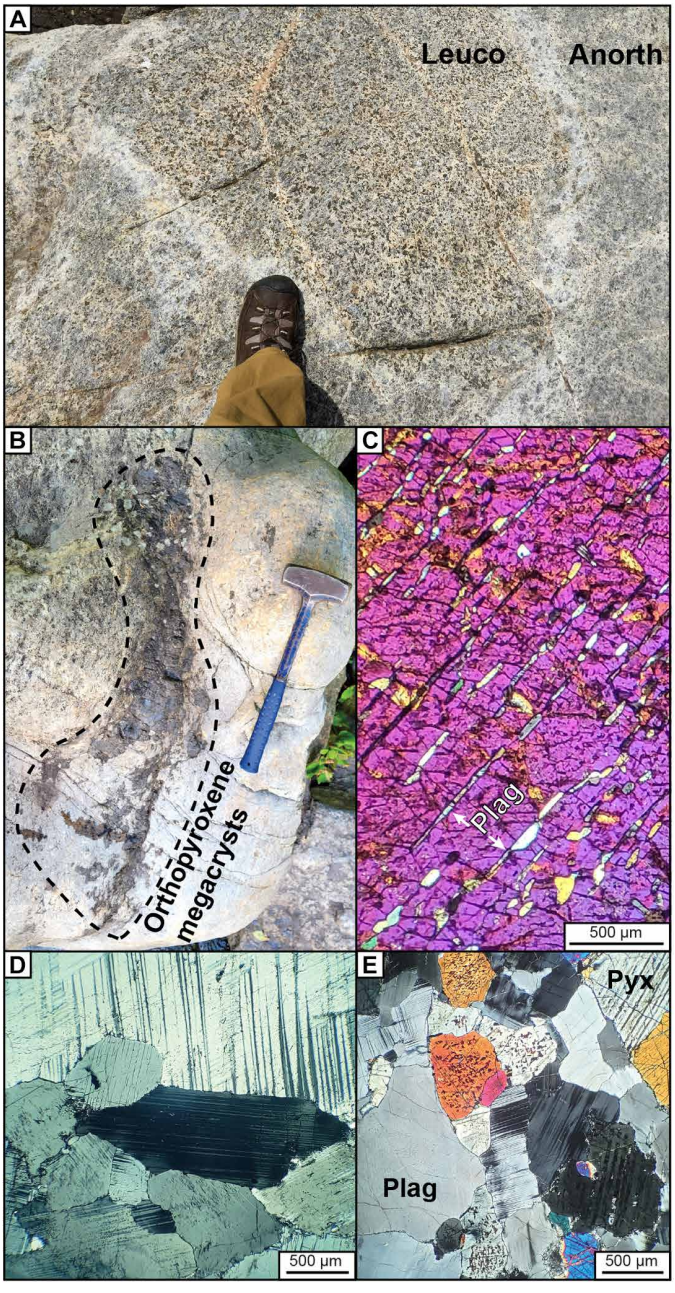

Fig. 2. Anorthosites and leucogabbros in outcrop and thin section. (**A**) Marcy outcrop (Wolfjaw Mountain) with a leucogabbro block (Leuco) in anorthosite (Anorth), showing that multiple generations of cumulate mushes coalesced to form the pluton. (**B**) Cluster of orthopyroxene megacrysts ~1 m in size in the Marcy anorthosite (Woolen Mill locality). (**C**) Clinopyroxene megacryst in thin section showing exsolved plagioclase (sample 98MA1A, crossed polars). (**D**) Coarse Marcy plagioclase in thin section (sample 14AD9A, crossed polars). (**E**) Pyroxene (Pyx) and plagioclase (Plag) in a Morin gabbroic anorthosite (sample 95MR115, crossed polars).

points to broadly closed-system behavior and limited fluid flow during metamorphism (*18*, *22*). For example, anorthosites from two lobes of the Marcy, constituting roughly half of its surface exposure, were estimated to have average $\delta^{18}O$ values of +9.3 ± 0.2 per mil (‰) [relative to Vienna Standard Mean Ocean Water (VSMOW); $N = 14$, 1σ SD] and + 9.6 ± 0.6‰ (VSMOW; $N = 23$, 1σ SD) from analyses of plagioclase megacrysts (*22*). Other than samples proximal to country rock contacts, including those with anomalously low $\delta^{18}O$ due to interactions with meteoric water during anorthosite emplacement (*10*), 83 of the 93 total Marcy anorthosites and leucogabbros/leuconorites that have been previously analyzed have $\delta^{18}O$ values between +8 and +11.2‰ (VSMOW) (*22*). Plagioclase from 48 representative rocks sampled from various parts of the western lobe of the Morin Complex, where the Morin samples of this study are also from, has an average $\delta^{18}O$ of +9.58 ± 0.67‰ (VSMOW; 1σ SD) (*18*). The known range of $\delta^{18}O$ values for the Morin western lobe is +8.5 to +12.1‰ (VSMOW) (*18*).

Rock samples for this study are Marcy and Morin anorthosites and leucogabbros. Sample locations are given in fig. S2. The Morin samples are from the relatively undeformed western lobe of the intrusion and were previously described and analyzed for oxygen isotopes (*18*). All rock samples contain coarse, glassy, igneous plagioclase up to ~4 cm that can show polysynthetic twinning and exsolution of K-feldspar and/or fine oxide particles. Labradorescence is visible in some plagioclase. Variable amounts of clinopyroxene and orthopyroxene, as well as oxide minerals, are present as intercumulus phases. Many pyroxenes show exsolution lamellae of Fe-Ti oxides and/or pyroxene (Fig. 2E). Also present are high-Al pyroxene megacrysts, which can contain exsolution lamellae of plagioclase and pyroxene (Fig. 2C). Such exsolved megacrysts, which have also been reported with oriented garnet lamellae (*23*), are thought to represent an early high-pressure pyroxene stable at ~10 kbar (*7*, *11*). Minor garnet and amphibole (<5 vol %), most commonly as coronal textures around pyroxene and Fe-Ti oxide, are present in some samples and are interpreted as metamorphic phases resulting from granulite facies metamorphism that postdated anorthosite intrusion by ~100 Ma (*20*). Some plagioclase shows minor alteration to fine-grained hydrous silicates along grain boundaries and cleavages (variably accompanied by amphibole and biotite), but these examples are visually apparent and were avoided when selecting materials for both in situ analysis and mineral separation.

Boron stable isotopes

Boron stable isotope analysis is a powerful tool for studying magmas formed at convergent margins because boron systematics can reveal inputs from the underlying subduction zone (*24*, *25*). Unaltered depleted mantle and mid-ocean ridge basalt (MORB) have $\delta^{11}B$ values of −7 ± 0.9‰, and the bulk continental crust has a $\delta^{11}B$ value of roughly −9 ± 0.4‰ (*24*, *26*). Rocks altered by seawater at low temperatures, such as LTAOC [$\delta^{11}B \approx -4$ to +25‰, 0.2 to ~100 parts per million (ppm) B] and the abyssal serpentinites underlying the oceanic crust ($\delta^{11}B \approx +2$ to +41‰, 2 to ~100 ppm B), are mostly enriched in B and have more positive $\delta^{11}B$ signatures relative to unaltered mantle and MORB (Fig. 3A) (*24, 26*). Fluids and melts derived from dehydrating slab-top materials impart distinctly enriched and/or isotopically heavy B signatures to modern arc magmas compared to bulk mantle and crustal reservoirs (Fig. 3A). Altered oceanic crust can also develop an isotopically lighter $\delta^{11}B$ signal than unaltered MORB after extensive subduction dehydration. As the slab top warms in the arc magma generation window between ~2 and 3 GPa, the fluids released by breakdown of hydrous silicates preferentially remove ^{11}B from the rock, resulting in the residual dehydrating slab becoming isotopically lighter (*27*, *28*). Forearc serpentinites and rocks from exhumed subduction zone mélanges with $\delta^{11}B$ signatures close to or below 0‰ are interpreted as metasomatic

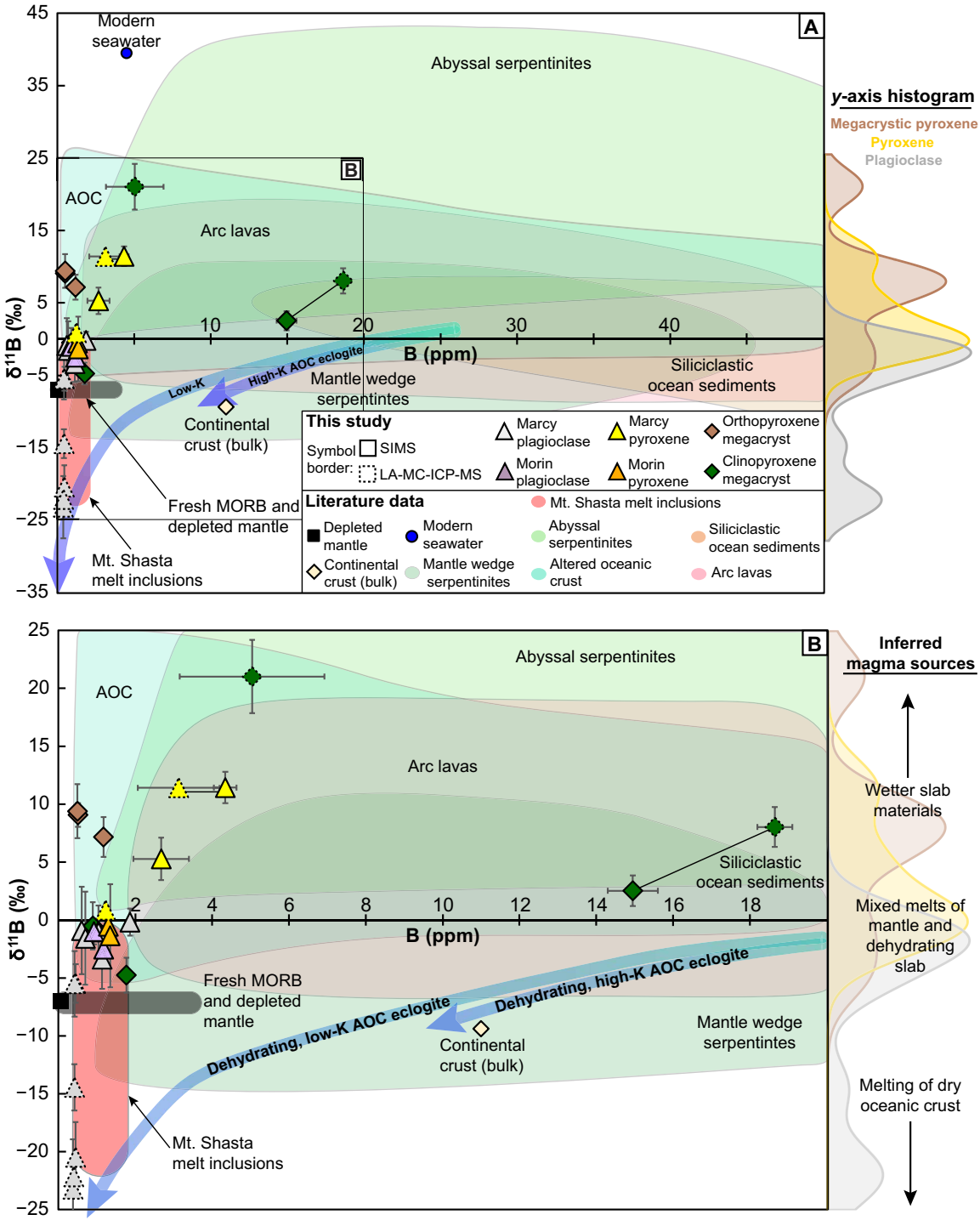

Fig. 3. Boron isotope systematics of the Marcy and Morin anorthosites. Symbols are averages of multiple measurements for each grain (tables S1 and S2). Error bars show ±2σ SE. Dehydration trends of eclogite are from (*28*); other references are given in Materials and Methods. Marginal histograms were calculated from grain averages using the default kernel smoothing in MATLAB (v.2020b); interlaboratory comparisons on the same grain were averaged for histograms. (**A**) Plagioclase and nonmegacrystic pyroxene show significantly higher and lower $\delta^{11}B$ values than bulk depleted mantle and continental crust and overlap with subduction zone lithologies. Pyroxene megacrysts can reach values similar to abyssal serpentinites. Plagioclase values closely resemble dehydrated slab eclogite and its melt(s) (*28*, *33*). Tie lines connect results for the same grain from SIMS and LA-MC-ICP-MS. (**B**) Detail of (A)'s left edge.

products formed by these slab-released fluids [e.g., (*29*, *30*, *31*, *32*)]. The residual high-temperature, volatile-poor eclogite is predicted to have a $\delta^{11}B$ signature ranging from −5 to −40‰ but very low B contents similar to those of unaltered MORB (*28*). This dehydrated eclogite can then impart its $\delta^{11}B$ signature to arc magmas during slab melting. For instance, olivine-hosted melt inclusions in Quaternary basaltic andesite from Mt. Shasta with $\delta^{11}B$ values ranging from −0.9 to −21.3‰ and low B concentrations of ≤1.6 ppm are interpreted as reflecting magma input from melting of dehydrated subducting oceanic crust in the hot Cascadia subduction zone (*33*).

To test for the presence of geochemical signals from subduction zone processes and lithologies, we analyzed the B concentrations and isotopic compositions of Marcy and Morin plagioclase, intercumulus pyroxenes, and pyroxene megacrysts. Subduction zone signals would be expected if the magmas parental to the anorthosites were generated above a subduction zone (such as in a continental arc system) but would not be expected from melting of mafic lower crust or melting of the mantle unrelated to subduction. In situ analyses were made on thin sections and pyroxene megacryst fragments mounted in epoxy using secondary ion mass spectrometry (SIMS) at Woods Hole Oceanographic Institution and laser ablation multicollector inductively coupled plasma mass spectrometry (LA-MC-ICP-MS) at the Lamont-Doherty Earth Observatory. All analytical procedures are given in Materials and Methods. The B isotope data for grain averages plotted in Fig. 3 are in table S1, and the individual analyses used to calculate grain averages are in table S2.

The B isotope systematics of Marcy and Morin igneous minerals are distinct from those of unaltered depleted mantle and bulk continental crust (Fig. 3). Clean, unaltered plagioclase is B poor (<2 ppm) and has $\delta^{11}B$ values ranging from ~0 to −25‰. This range of $\delta^{11}B$ values matches subducting eclogite at varying stages of dehydration (*28*) and melts thought to be derived from dehydrated slab eclogite (*33*). Unaltered pyroxene megacrysts show values between approximately −5 and +21‰, similar to AOC, siliciclastic ocean sediments, and abyssal serpentinites. Nonmegacrystic pyroxenes are enriched in B compared to plagioclase (~1 to 5 ppm) and have $\delta^{11}B$ values between approximately −3 and +12‰, overlapping with both plagioclase and megacrystic pyroxenes. The $\delta^{11}B$ values of an approximately +33‰ altered pyroxene megacryst, and a +12‰ pyroxene was reproduced within analytical uncertainty by both SIMS and LA-MC-ICP-MS analyses on the same grain, confirming that both methods return similar results (table S1).

We also measured the major element compositions of plagioclase and pyroxene grains analyzed for B isotopes by SIMS using electron probe microanalysis (EPMA; Materials and Methods). The EPMA analyses were made within ~100 μm of SIMS spots. The EPMA analyses showed that each grain in tables S1 and S2 not labeled as "altered or uncertain" has a primary, unaltered composition within the expected ranges of primary plagioclase and pyroxenes from the Marcy or Morin (tables S3 and S4) (*1*, *16*, *23*, *34*–*37*). This is strong evidence that the grains plotted in Fig. 3 are unaltered and representative samples from the two massifs.

Nd, Sr, and O isotopes

As additional tests of possible slab contributions to the anorthosite parental magmas, we also analyzed radiogenic neodymium and strontium isotopes and stable oxygen isotopes of plagioclase. These systems have previously been applied to the Marcy and Morin, as well as to other massif-type anorthosites, to constrain the influence of mantle and crustal lithologies on their parental magmas (*10*, *18*, *22*, *38*, *39*). We build upon this previous work with new Nd, Sr, and O isotope data for Marcy and Morin plagioclase separates. Following mineral separation, analyses of Nd and Sr isotopes were conducted using MC-ICP-MS at the Radiogenic Isotope and Geochronology Laboratory (RIGL) at Washington State University. Analyses of O isotopes were conducted using laser fluorination at the University of Wisconsin-Madison. Analytical techniques and notation details are given in Materials and Methods. Neodymium, Sr, and O isotope data for Marcy rocks are in table S5 and for Morin rocks are in table S6.

Because the Marcy and Morin intrusions both formed at ~1155 Ma (*20*, *21*), their radiogenic isotope systematics can be directly compared. Anorthosites, leucogabbros, and gabbros from both massifs have ε_{Nd} values between +1 and +5 that approach, but are somewhat lower than, depleted mantle values at the age of formation (+5.4) (*40*), suggesting that the parental magmas were influenced by both mantle and crustal sources (Fig. 4A) (*18*). Many of the rocks have only slightly lower ε_{Nd} values than oceanic crust ~200 Ma older than the anorthosites, such as might be present in a subducting slab. Strontium systematics show a similar pattern with some samples plotting near 200 Ma older LTAOC and others showing variable spread toward more evolved values (Fig. 4B). Particularly for the Rb-Sr system, this spread may be the result of resetting during the Ottawan orogeny ~100 Ma after anorthosite emplacement (*38*).

Analyzed plagioclase separates from Marcy and Morin anorthosites and gabbroic anorthosites have $\delta^{18}O$ values of +8.6 to +10.7‰ (VSMOW), consistent with prior studies of these massifs (*18*, *22*, *41*). Marcy gabbros have $\delta^{18}O$ as high as +9‰ but also show primary igneous values as low as +6.5‰ (*22*). The dominant plagioclase signature of roughly +9‰ $\delta^{18}O$ is much higher than the ~+5.75‰ value expected for basaltic melt derived from an unaltered upper mantle source, and small O isotope fractionations at high temperatures preclude magmatic derivation from mantle rocks alone (*42*). High $\delta^{18}O$ values ≈ +9‰ are consistent with input from rocks altered by seawater at ≤400°C, such as slab-top LTAOC (*18*, *43*). The oxygen isotopic composition of plagioclase, the dominant mineral in the rock, approximates the oxygen isotope ratio of the whole rock.

The O isotopic compositions of the Marcy and Morin show little variation at the massif scale other than local anomalies at contacts with country rock, which is evidence that the parental magmas to the plagioclase cumulates did not acquire their $\delta^{18}O$ signatures during emplacement but rather inherited them from the deeper magmatic system that fed the intrusions (*18*, *22*). Our O and Nd isotope data cluster tightly with results from previous studies (*18*, *22*, *38*) and, although the Sr isotope data show some spread and possible metamorphic resetting, the most juvenile values cluster in a similar manner to the Nd data (Fig. 4B). Measured Rb and Sr contents of Marcy and Morin plagioclase (tables S5 and S6) are consistent with the extensive published bulk rock analyses for these massifs (*35*, *36*, *44*). Although many fewer Sm and Nd data are available for the Marcy and Morin, our results are consistent with published plagioclase ranges (*35*, *38*, *45*). This is further evidence that our samples are representative.

Evaluating possible parental magmas

Previous studies have used Nd, Sr, and O isotopic signatures to identify possible sources of—and contaminants to—the magmas parental to different anorthosite massifs by modeling source mixing and/or crustal assimilation [e.g., (*18*, *38*, *46*–*50*)]. To evaluate possible

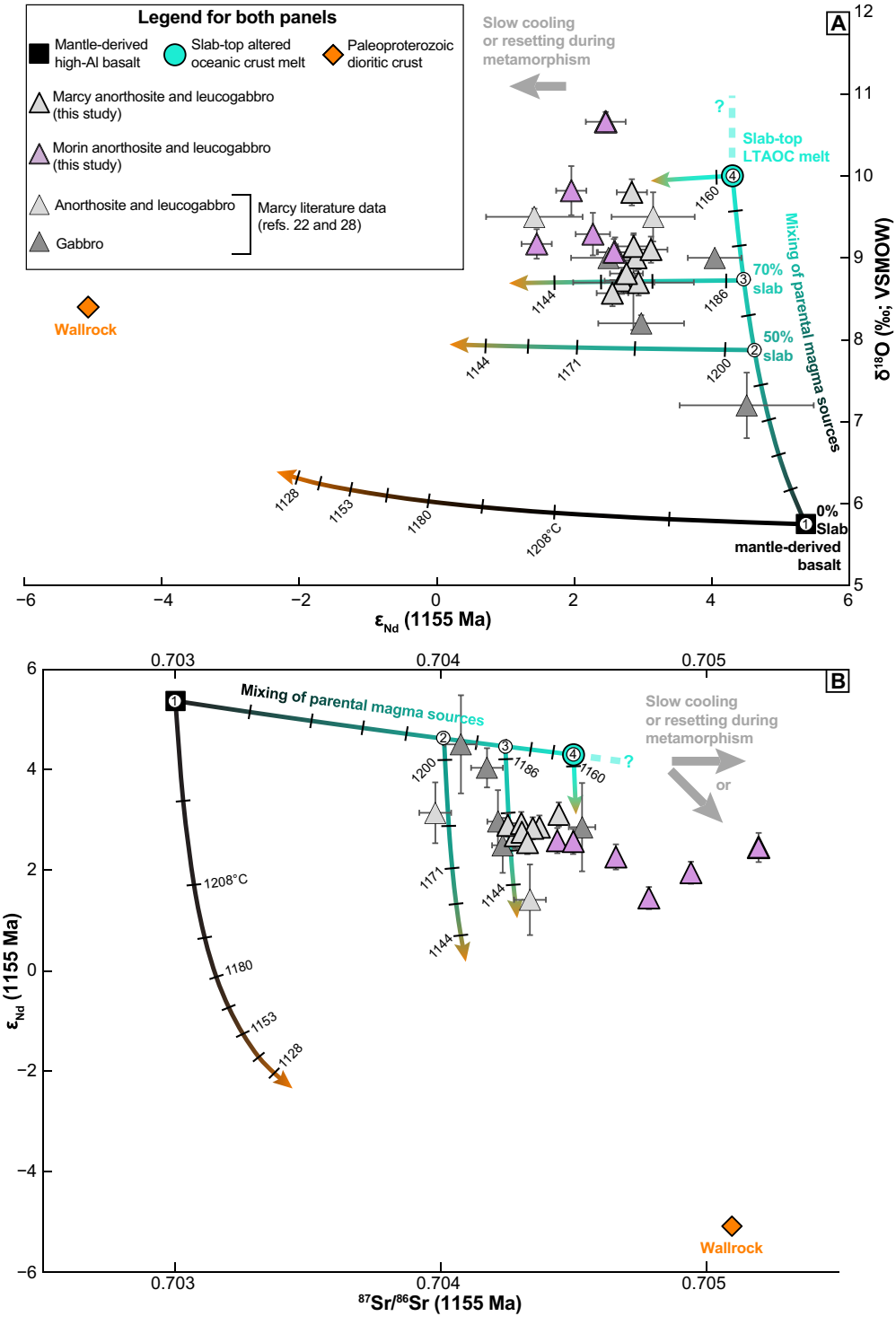

Fig. 4. Marcy and Morin Nd-Sr-O systematics compared to Magma Chamber Simulator model results. Candidate parental magmas #1 to #4 with differing proportions of LTAOC melt and mantle melt are shown undergoing wallrock assimilation and fractional crystallization. Major element trends and mineralogy of these simulations are shown in Fig. 5. Curves show magma isotopic composition until the magma reaches 56 wt % SiO_2 (arrowhead tips); tick marks are labeled by temperature (°C). Curves are qualitatively shaded to indicate source influence. Model setups are given in Materials and Methods. Error bars are ±2σ SE. (**A**) Nd-O plot. Assimilation of wallrock by mixed mafic melts derived from slab LTAOC and mantle sources fits the data well, but mantle-derived basalt assimilating wallrock alone does not. Neodymium isotope data from (*38*) have been normalized to $^{146}Nd/^{144}Nd = 0.7219$, and those Nd and Sr data have been recalculated for an age of 1155 Ma. (**B**) Sr-Nd plot.

contributions from LTAOC to the Marcy and Morin parental magmas, we combined the Nd, Sr, and O isotope data with compiled literature data on bulk rock chemistry from these massifs. We compared these data to results from numerical modeling of magma crystallization and wallrock assimilation using both the Magma Chamber Simulator software, which tracks bulk composition, cumulate mineralogy, isotopic composition, and physical properties (*51*, *52*), and classical algebraic assimilation-fractional crystallization (AFC) models (*53*, *54*) to evaluate processes that could have produced the observed systematics. All simulations were conducted at 10 kbar; our analysis focuses on the mineralogy and chemistry of the cumulus phases and the magma from which they crystallized at near-Moho depths and does not address later fractional crystallization or polybaric processes during anorthosite emplacement. We focus on the early lower-crustal magmatic evolution of the system because of the evidence that the parental magmas acquired their isotopic signatures at this stage (*18*, *22*) and because the entrainment of high-Al pyroxene megacrysts in the anorthosites indicates plentiful plagioclase crystallization at pressures near 10 kbar (*7*, *11*). Our approach follows previous work that showed that the petrological evolution of massif-type anorthosite parental magmas, including those of the Marcy, can be explained by assimilation of the lower crust at ~10 kbar followed by polybaric fractional crystallization with lesser assimilation as the magmas and cumulates ascend (*8*). Details of modeling setups are given in Materials and Methods.

To model the Nd, Sr, and O isotopic signatures of the magmas parental to the anorthosites, we treated the mantle, crustal, and LTAOC lithologies and their melts as distinct, but homogeneous, isotopic reservoirs (table S7). This approach is justified because even accounting for different temperatures of melting along slab depth, the Nd, Sr, and O isotopic characteristics of LTAOC are thought to change minimally during metamorphism, as evidenced by preserved AOC-like signatures in Archean eclogite xenoliths erupted by kimberlites (*55*). However, the B isotopic composition of LTAOC is extremely sensitive to the extent of devolatilization during subduction (*28*), and possible reservoirs such as serpentinite can show a wide range of $\delta^{11}B$ values and B concentrations [e.g., (*32*)]. Because the different lithologies that might contribute B to the parental magma cannot be treated as homogeneous reservoirs in the geologic scenarios relevant to massif-type anorthosite formation, we did not include B isotopes in our numerical modeling. However, more complex B modeling could be explored in future work.

We tracked the AFC evolution of four different candidate parental magmas: a pure mantle-derived basalt endmember capable of producing massif-type anorthosite mineralogy (*8*) (#1), a mixed magma consisting of 50% LTAOC melt and 50% mantle-derived basalt (#2), a mixed magma consisting of 70% LTAOC melt and 30% mantle-derived basalt (#3), and a pure LTAOC melt endmember (#4). The major element, trace element, and isotopic compositions of these parental magmas and the assimilated wallrocks are given in table S7. Wallrock compositions were taken from a global compilation of lower crustal xenoliths that have been analyzed for major and trace element chemistry and oxygen isotopes (table S8) (*56*). The LTAOC represents the altered upper kilometer of subducting ocean crust (e.g., pillow basalts and sheeted dikes), chosen to be 200 Ma older than the anorthosite parental magmas to represent plausible seafloor that would have been subducting during Grenville convergence. The LTAOC has slightly lower ε_{Nd} than basaltic magma derived from 1155 Ma depleted mantle because of its older age and has higher $\delta^{18}O$ and $^{87}Sr/^{86}Sr$ because of its low-temperature alteration by seawater (*43*). All magmas were placed into contact with a Paleoproterozoic dioritic wallrock, calculated from the average of lower crustal xenoliths of intermediate SiO_2 content (*56*). The isotopic evolution, major element chemistry, and cumulus plagioclase properties of the four candidate parental magmas can be compared across Figs. 4 and 5. We also modeled the Nd-Sr-O evolution of these magmas using an algebraic AFC approach that does not consider thermodynamics and dynamic phase equilibria (*53*, *54*). This approach produces extremely similar isotopic evolutions of the parental magmas to the Magma Chamber Simulator results (fig. S3 and table S7). Further details of model setups are given in Materials and Methods. Tables S10 to S15 contain the Magma Chamber Simulator run inputs and outputs, including major element, trace element, and isotopic compositions (the Supplementary Materials).

The isotopic evolution of candidate parental magmas #2 to #4 during AFC best reproduces the Nd-Sr-O systematics of the Marcy and Morin anorthosites, leucogabbros, and gabbros. Without LTAOC input, none of the average lower crustal wallrock compositions (mafic, intermediate, and metasedimentary/felsic) can raise the parental magma $\delta^{18}O$ to +9‰ (figs. S4 and S5).

Figure 5 shows the magma major element composition and cumulus plagioclase properties of candidate parental magmas #1 to #4 during fractional crystallization and wallrock assimilation. The starting magma compositions of the four candidate parental magmas are all basaltic (47 to 53 wt % SiO_2) and Al-rich (17 to 20 wt % Al_2O_3) and closely resemble suggested Marcy parental magmas inferred to have ~52 wt % SiO_2 (*34*). A 52% partial melt of a MORB-like eclogite from an experimental study of high-T MORB melting (*57*), used here to represent extensive melting of AOC that has undergone prograde dehydration, plots within the composition range of Marcy and Morin gabbros and represents candidate parental magma #4. We tested a mafic melt of a MORB source because of the similarities between the Nd, Sr, and O isotopic compositions of Marcy and Morin anorthosites, leucogabbros, and gabbros and those of LTAOC (Fig. 4). Together with mafic bulk compositions and B isotopic compositions reflecting influence from AOC, these traits point to a mafic parental magma with geochemistry similar to oceanic crust. Parental magmas containing a 50 to 100% LTAOC melt component that undergo fractional crystallization and wallrock assimilation can produce gabbros, gabbroic anorthosites, and anorthosites matching Morin and Marcy compositions in terms of major elements, trace elements, and Nd, Sr, and O isotopes (Figs. 4 and 5, A and B). Plagioclase Nd and Sr concentrations are also closely reproduced by the AFC evolutions of candidate parental magmas #2 to #4 (fig. S6). The highest plagioclase Nd concentrations can be explained by mixing of recharging magma batches with fresh magma or equilibration during late-stage fractional crystallization.

Addition of LTAOC melt also influences the onset of plagioclase crystallization and plagioclase chemistry and so has implications for the buoyancy of plagioclase cumulates necessary to facilitate massif-type anorthosite formation. Candidate parental magmas #2 to #4 produce plagioclase cumulates matching the observed composition ranges of the Marcy and Morin. The mineral and melt densities from these simulations show that the plagioclase cumulate is positively buoyant relative to the coexisting magma at the simulation pressure of 10 kbar (Fig. 5C). This is likely the result of

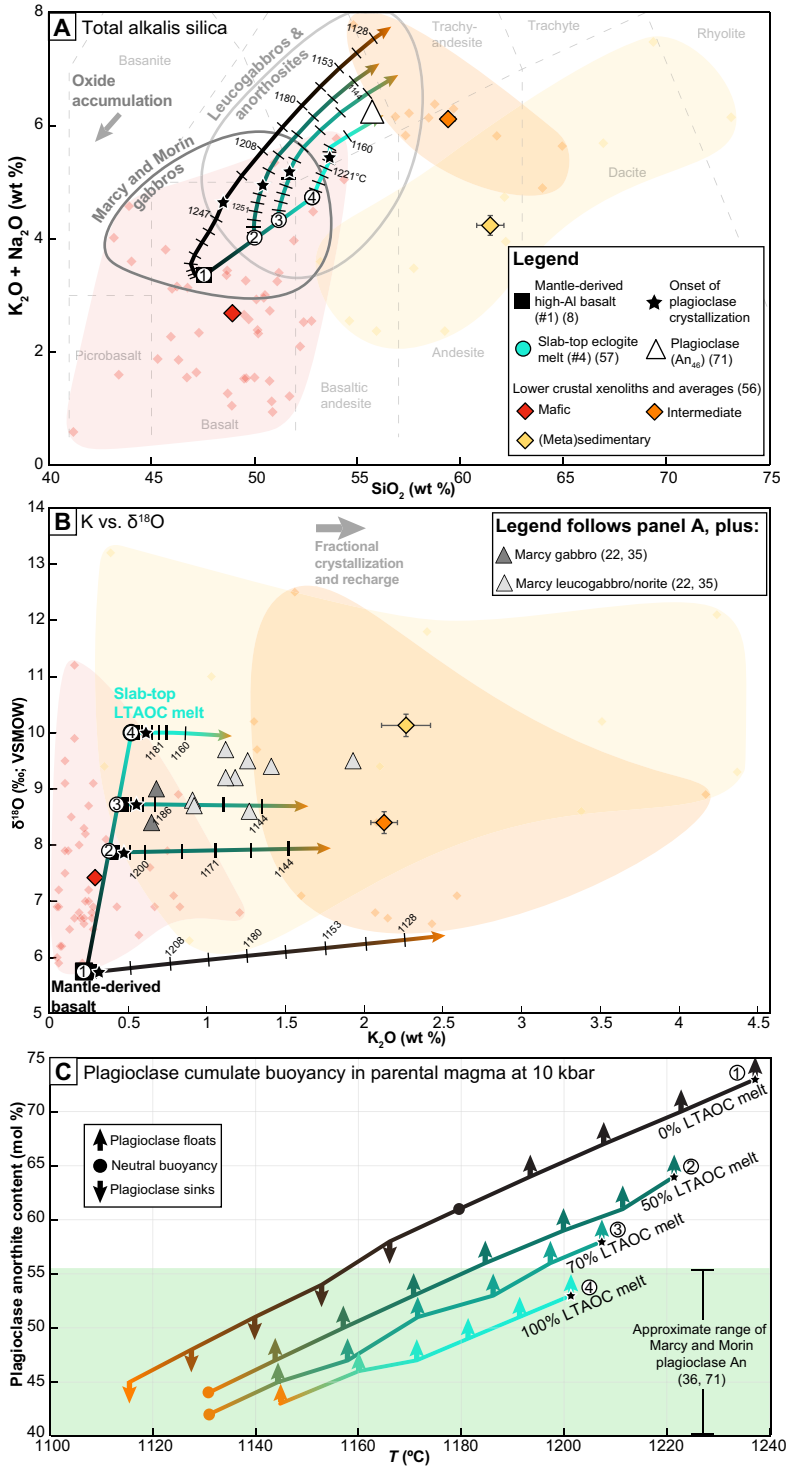

Fig. 5. Marcy and Morin rock bulk compositions and plagioclase compositions compared to Magma Chamber Simulator model results. Candidate parental magmas #1 to #4 are shown undergoing AFC processes. Stars show the onset of plagioclase crystallization. Other details as in Fig. 4. (**A**) Total alkali silica diagram. Addition of plagioclase (white triangle) to the gabbro compositions produces anorthositic gabbros and anorthosites. (**B**) Magma K_2O versus $\delta^{18}O$ for the same simulations. (**C**) Plagioclase composition and buoyancy for the same simulations at 10 kbar.

a higher Na/Ca ratio in the parental magmas containing eclogite melt, which stabilizes plagioclase with lower An content and therefore lower density, earlier in the crystallization sequence. Simulations #2 to #4 crystallize plagioclase of the appropriate composition when the magma chamber still contains >50% magma, which should enable plagioclase to float and form anorthosite.

DISCUSSION

Interpreting the B and O isotope data

We consider it appropriate to interpret the $\delta^{11}B$ compositions of the Marcy and Morin minerals in the same way that modern B systematics are interpreted because marbles both in contact with the Marcy anorthosite in the Adirondack Highlands and in the nearby Adirondack Lowlands have $\delta^{11}B$ values within the range of modern oceanic carbonate (*58*). This suggests that the seawater in which the Adirondack metasedimentary protoliths formed had a generally similar $\delta^{11}B$ composition to modern seawater and therefore that the B isotopic signatures of seafloor hydrothermal alteration should be broadly similar.

Both SIMS and LA-MC-ICP-MS analyses show pyroxene and plagioclase in the same thin section with $\delta^{11}B$ values differing by 20‰ or more. At least for sample 14AD9A, in which the largest number of grains was analyzed, the $\delta^{11}B$ variability within single plagioclase and pyroxene grains is less than the variability among grains of that mineral in the sample. These pieces of evidence suggest that diffusional B exchange between mineral grains was inefficient, even during the granulite facies metamorphic overprint of the Ottawan orogeny (*20*). This could be the result of large grain sizes and scarcity of grain boundary fluids during mostly dry metamorphism that restricted B transport to solid-state intragranular diffusion, which should be slower than diffusion through fluids or melts. It is also possible that the trace B in the silicate structures is coupled to slow-diffusing species or diffuses slowly itself. Similar behavior has been observed for Li in quartz associated with substituted Al (*59*) and for P in garnet, which can remain immobile even during metamorphism at ≥1050°C in the absence of fluid-mediated recrystallization (*60*, *61*). In the absence of published experimental constraints on B diffusion in plagioclase and pyroxene, further study is required to understand B mobility in these phases.

The equilibrium preference of ^{11}B for trigonal coordination and ^{10}B for tetrahedral coordination causes the proportion of trigonally coordinated and tetrahedrally coordinated B in a mineral to affect its B isotopic composition (*62*, *63*). Boron in plagioclase is thought to be dominantly tetrahedrally coordinated and accommodated by the reedmergnerite substitution of B for Al, which is tetrahedrally coordinated (*64*). Although B in inosilicates has also often been assumed to be tetrahedrally coordinated, spectroscopic study of synthetic diopside has shown a strong dominance of trigonally coordinated B, which would produce an enrichment in ^{11}B and a higher $\delta^{11}B$ value because of the tendency of trigonal coordination to favor the incorporation of ^{11}B over ^{10}B (*62*, *63*). This effect has not yet been documented in orthopyroxenes. At the high magmatic temperatures relevant to the crystallization of the plagioclase cumulates that formed the anorthosites (~900° to 1250°C), the magnitude of the temperature-dependent equilibrium isotope effect is estimated to be ≤ ~5‰ (*62*). Incorporation of trigonally coordinated B in pyroxenes but not in feldspars likely helps to explain the generally higher $\delta^{11}B$ values of pyroxenes relative to feldspars but appears insufficient to explain the ranges of values observed within plagioclase, intercumulus pyroxenes, and megacrystic pyroxene populations and cannot explain the ~40‰ range observed overall (Fig. 3). Instead, material sourced from different reservoirs related to a subduction zone, which can have $\delta^{11}B$ signatures that differ by this magnitude or more (*24*, *32*, *65*), appears to be required.

Metasomatism of the subarc mantle by slab-derived fluids alone cannot explain the Marcy and Morin $\delta^{18}O$ signature because of the extreme water-rock ratios that would be required to raise the subarc mantle $\delta^{18}O$ to roughly +9‰. The low water activity of the anorthosite parental magmas indicated by plagioclase compositions and lack of magmatic amphibole (*1*, *8*) means that only small amounts of fluids could have been integrated into the parental magmas. High magma water contents would also limit plagioclase buoyancy and, therefore, anorthosite formation, by reducing magma density. Moreover, massif-type anorthosites do not form in modern settings where mantle metasomatism by slab-derived fluids is thought to be common, implying that mantle metasomatism is not a causative mechanism for massif-type anorthosite formation.

Synthesis of observations

Overall, we interpret the B isotope data as indicating input from several lithologies expected in a subduction zone environment, mostly corresponding to AOC-like signatures and slab-top siliciclastic sediments but also including serpentinites (Fig. 3). The range of plagioclase $\delta^{11}B$ values is nearly identical to that observed in olivine-hosted melt inclusions interpreted as mixed melts of dry, subducted oceanic crust and a mantle wedge above a hot subduction zone (Fig. 3) (*33*). Metasomatism of the subarc mantle by slab-derived fluids probably affected the B isotopic compositions of the parental magmas but cannot by itself explain the observed $\delta^{18}O$ signatures of the cumulus phases and the low water activity of the parental magmas. Texturally early pyroxene megacrysts with $\delta^{11}B$ values ranging from −5 to +21‰ may reflect early influence of slab-derived fluids on the mantle wedge and/or magmatic system.

Scenarios without LTAOC melt in the parental magma (e.g., candidate parental magma #1 in Figs. 4 and 5), regardless of wallrock type, fail because they cannot produce the approximately +3 ε_{Nd}, +9‰ $\delta^{18}O$ anorthosites and gabbros, and/or fail to match the observed mafic, yet high $\delta^{18}O$, gabbros (Figs. 4 and 5 and figs. S4 and S5). Metasediments with $\delta^{18}O >>$ 10‰ could theoretically sufficiently raise parental magma $\delta^{18}O$, but more than ~10% mass input from melts of any common metasedimentary rock types into the parental magma is incompatible with the mineralogy and bulk compositions of the anorthosites and related rocks (Fig. 5A). Even if large amounts of metasediment with $\delta^{18}O$ of +20‰ had been present in the lower crust during parental magma crystallization, close to 40% of the parental magma's volume would have to be derived from this material to produce anorthosites with $\delta^{18}O$ of +9 to 10‰. Furthermore, to reproduce the observed natural data, the metasediment would have to have an ε_{Nd} signature similar to that of the depleted mantle at 1155 Ma, which is improbable. Large input from siliciclastic metasediments, which are generally enriched in Rb (table S8), is also precluded by the low Rb contents of the Marcy (table S5) (*22*) and Morin (table S6) plagioclase. Candidate parental magma #1 with only mantle-derived basalt also does not produce plagioclase cumulates corresponding to the compositions observed in the Marcy and Morin (~An_{39} to An_{56}) that float in the parental magma (Fig. 5C). Any scenarios without LTAOC also must explain the range of observed plagioclase $\delta^{11}B$ values spanning ~0 to −25‰ (Fig. 3).

We conclude that mixing of mantle wedge melts with basaltic melts derived from LTAOC that had already undergone some prograde dehydration, accompanied by minor fluid input from other subduction zone lithologies, is the simplest explanation that satisfies the constraints from the radiogenic and stable isotope systematics and bulk compositions of the magmas parental to the Marcy and Morin.

A slab melting model for massif-type anorthosite genesis

The Marcy and Morin share several characteristic traits with most other massif-type anorthosites (*4*, *34*). They are dominated by anorthosite and anorthositic gabbros, norites, and/or troctolites with plagioclase between An_{30} and An_{60}, contain rare pyroxene megacrysts variably containing exsolved plagioclase (±pyroxene and garnet), have few to no primary hydrous phases, show multiple cross-cutting anorthosite generations in outcrop, and were emplaced into a Proterozoic convergent margin. Although the Marcy and Morin have higher $\delta^{18}O$ values than most other massifs (*41*), we conclude—because of the many other similarities—that the processes that formed the Marcy and Morin were probably similar to those that produced many other massifs and contemporaneous felsic plutons (the Mangerite-Charnockite-Granite association with anorthosite). Building upon evidence that mafic melts of slab-top LTAOC are required to explain the isotopic and major element systematics of the Marcy and Morin, we present a model for massif-type anorthosite genesis that can be tested for other massifs worldwide (Fig. 6).

Massif-type anorthosites predominantly formed during assembly of Proterozoic supercontinents or underneath supercontinents that had not yet broken apart (Fig. 1). The Marcy and Morin formed along a convergent margin during assembly of the supercontinent Rodinia (*16*), a setting that could facilitate both mantle and slab melting. Formation of the Marcy and Morin, and that of other massifs, has long been linked to tectonically driven disruptions to background geotherms, such as asthenospheric upwelling (*1*, *16*). We propose that processes capable of bringing upwelling aesthenosphere into contact with a slab, such as lithospheric delamination, slab rollback, or slab breakoff, may have been key to producing massif-type anorthosites. Some of these processes may have been triggered by interactions or collisions of multiple slabs underneath an assembling supercontinent, as would be expected if a "subduction girdle" brought slabs into contact along the supercontinent's edges (*66*). Thermal insulation by the supercontinent (*67*) would be expected to raise the temperatures of subducting slabs and could help explain why massif-type anorthosites predominantly formed during supercontinent assembly. Slowdown of tectonic plate speeds, inferred during the Proterozoic (*5*), could also have facilitated hotter slab tops by enabling more efficient thermal equilibration of the downgoing plate with the mantle.

We propose that a distinctive tectonic regime or conditions associated with Proterozoic subduction might be responsible for the genesis of massif-type anorthosites, but note that melt generation above subducting slabs in the Proterozoic could still produce arc magmatism similar to Phanerozoic examples. For example, basement rocks to the Marcy and Morin anorthosites are typical 1.4 to 1.3 Ga calc-alkaline tonalites and granodiorites with arc affinities (*68*, *69*), and a

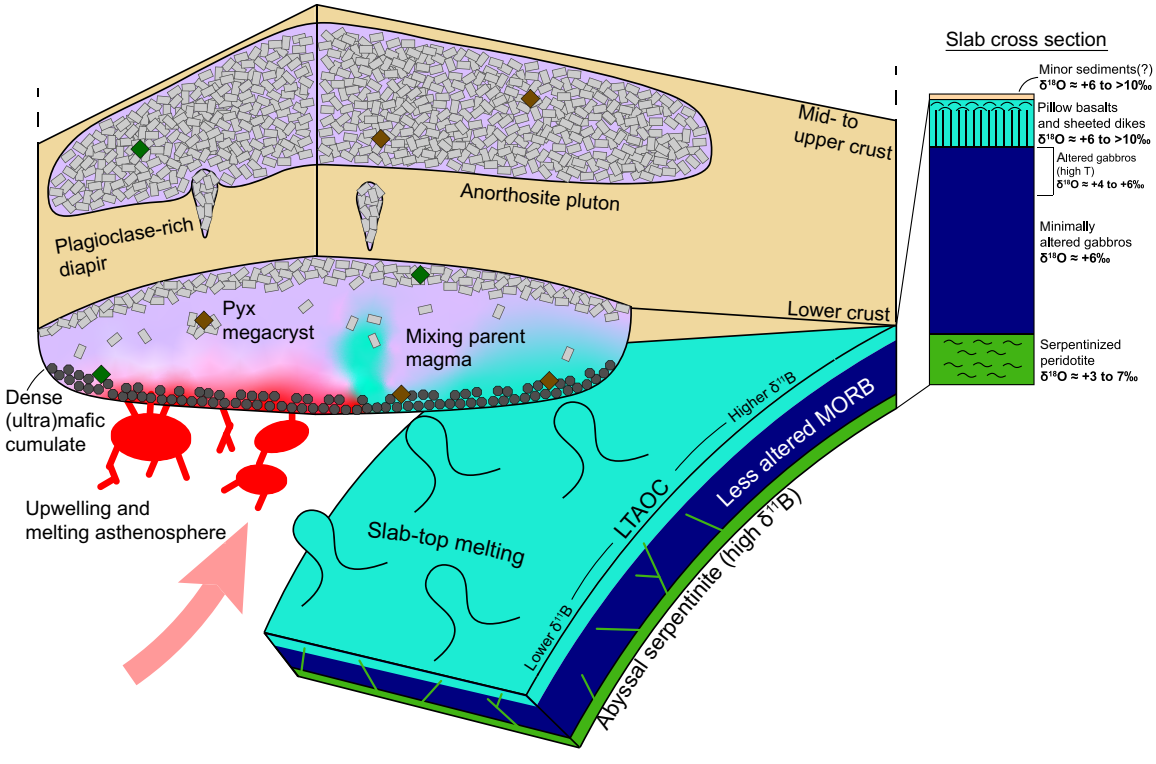

Fig. 6. Proposed model for the formation of the Marcy and Morin massif-type anorthosites. Isotope systematics and bulk compositions of anorthosites and associated mafic rocks point to melting of slab-top LTAOC that had dehydrated to various degrees before melting. Upwelling asthenosphere provides a heat source to melt the slab and likely melted to provide additional mafic magma. Texturally early pyroxene megacrysts do not show $\delta^{11}B$ values lower than those of unaltered mantle, suggesting that early slab-derived fluids and sediment melts also contributed to their formation. Varied $\delta^{11}B$ signals within one rock likely record changes to magma sources from different slab depths through time (*28*) or mixed cumulate populations. Oceanic crust cross section is after (*43*).

bimodal calc-alkaline suite of 1.20 Ga plutons marks the closure of the Trans-Adirondack back-arc basin immediately preceding 1.15 Ga anorthosite magmatism (*70*). The spatial and temporal associations between these rock types suggest that anorthosite magmatism in the Adirondacks may represent either a thermal disruption to typical arc-related magmatism or perhaps may have been related to its termination.

For the Marcy and Morin, we posit that lithospheric delamination or slab rollback is a better fit than slab breakoff for initiating mantle upwelling because of the large amount of high-$\delta^{18}O$ material present in their source(s). Slab breakoff would likely expose a deeper cross section of the slab to melting, which would produce magmas with a lower integrated $\delta^{18}O$ by sourcing melts from both LTAOC (high-$\delta^{18}O$) and deeper, unaltered (mantle-like $\delta^{18}O$) oceanic crust (*43*). Many massifs have $\delta^{18}O$ of approximately +7‰ (*41*); these could be explained by slab melting that sampled a deeper transect of oceanic crust. Because even small amounts of AOC or serpentinite- or sediment-derived fluids assimilated into the parental magma can shift $\delta^{11}B$ values outside of the mantle range [e.g., (*65*)], B isotope studies of more massifs can test this hypothesis.

The deep parental magma chambers to massif-type anorthosites were probably refilled by multiple recharge pulses, which would explain the observed longevity of some anorthosite-producing systems (*9*, *13*), the enormous volumes of plagioclase cumulates with a restricted range of anorthite contents (An_{39} to An_{56}) (*71*), and some of the observed spread in Nd-O isotope systematics (Fig. 4A). Melting of slab-top LTAOC that had undergone various stages of dehydration would produce the observed range of plagioclase $\delta^{11}B$ values (Fig. 3), although mixing of cumulate populations from different melt batches could also produce a range of $\delta^{11}B$ values. The presence of a subducting slab underneath the anorthosite-forming system may have provided a continual influx of fresh material to melt over the duration of magmatism. Mixing of hot, buoyantly upwelling fresh magma injections with fractionally crystallizing residual magma might have provided a physical impetus for plagioclase diapir ascension.

Implications for Earth's evolving magmatic regimes

While slabs may melt to small or even moderate degrees along modern subduction zone thermal regimes (*72*, *73*), our results point to much larger degrees of melting during the Proterozoic, a time when plate tectonics likely resembled modern regimes, but the upper mantle was hotter [e.g., (*74*, *75*)]. This could explain a longstanding mystery about massif-type anorthosites: their restriction to the middle part of Earth's history. Our findings imply that massif-type anorthosites would be expected to form on a tectonically active planet with a hot mantle where subducting slabs undergo intense melting underneath continental crust. High upper mantle temperatures should produce efficient devolatilization of the subducting slab at shallow depths, resulting in relatively dry slab melts at subarc depths. Although common in Proterozoic convergent settings during supercontinent assembly, massif-type anorthosites do not appear to have formed during the Phanerozoic assembly of Pangea or since. If slab melting made massif-type anorthosites, then their production should have declined as the mantle cooled and oceanic crust in subduction zones melting thoroughly enough to produce basaltic magmas became rare or ceased entirely. The absence of massif-type anorthosites older than the Neoarchean may be the result of a different style of tectonics [e.g., (*75*, *76*)] or of differences in plate thickness, temperature, and/or velocity (*4*, *5*). Any one of these factors would likely affect the mechanics of convergent margins and the feasibility of long-lived mafic magma systems at approximately Moho depths with lifetimes long enough to segregate large plagioclase cumulate accumulations.

MATERIALS AND METHODS

Samples

Rock samples of anorthosite and associated plagioclase-rich rocks (e.g., leucogabbro) were sourced from material collected for prior work (*77*, *78*).

Boron isotope analysis and sample preparation

For B isotope analyses, petrographic thin sections were prepared using alumina grit rather than diamond paste due to the B contamination hazard posed by diamonds (*79*). Before SIMS analysis, 1″ diameter polished sections were cleaned in an ultrasonic bath first with deionized water and then with Milli-Q H_2O for 10 min at each stage and then dried in an oven at ~40°C before gold coating.

One set of boron isotope analyses was performed at Woods Hole Oceanographic Institution using the Cameca IMS 1280 SIMS in the Department of Geology and Geophysics. Analytical methods followed those in (*79*). Analyses used a 12-keV $^{16}O^-$ primary ion beam, ~50- to 80-nA beam current, 10-kV secondary acceleration voltage, a 4000 μm by 4000 μm field aperture, and produced a ~50- to 100-μm-diameter beam spot. Sample surfaces were presputtered for 300 to 500 s before analysis, followed by counting $^{10}B^+$(15 s), $^{11}B^+$ (5 s), and ^{28}Si++ (1 s) over 40 cycles in monocollector mode using an electron multiplier. Total analysis time for each spot was 32 min. The relatively high primary beam current was necessary for transmitting sufficient signals of $^{10}B^+$ and $^{11}B^+$ to generate counting statistics for adequately precise ratios on grains with B (<1 μg/g). The strong primary beam, combined with a relatively long presputtering time, sputtered through potential surface B (contamination) before measurement. In addition, the 4000 μm by 4000 μm field aperture blocked the transmission of secondary B^+ ions from outside of the innermost 40 μm by 40 μm from the center of the crater during analysis, thereby minimizing the transmission stray surface B^+ ions from the crater periphery. Analysis of Boron-free Herasil glass on the standard mount produced <5 counts/s $^{11}B^+$ ions and <1 count/s $^{10}B^+$, demonstrating that the analytical setup effectively negated surface background contamination on cleaned, well-polished surfaces. The primary standard used between samples was GOR132 in session one and StHs6/80 in session two, with GOR132, GOR128, B6, StHs6/80, and NIST612 used as standards for calibrations. Comparison of instrumental mass fractionation factors between mafic GOR128 and GOR132 and andesitic StHs6/80 shows no matrix dependence on instrumental mass fractionation, as previously demonstrated (*79*). Fractionation factors of these three glasses were within error and reproducible to 1.2‰ relative standard deviation (RSD; 2σ). Fractionation factors were smaller than those previously determined by SIMS for a range of glasses and salts concluded to represent negligible matrix effects (*80*). The NIST612 standard, which was also used for LA-MC-ICP-MS analyses (see below), has been confirmed to produce similar $\delta^{11}B$ values by SIMS and positive thermal ionization mass spectrometry (*81*). Analyses of megacrysts in all samples except 14AD9A were conducted from crystal fragments mounted in epoxy with standards; all other analyses were conducted

in situ using 1″ round thin sections. Standards produced identical results within analytical uncertainty when analyzed in the epoxy mount compared to an indium mount. Using the SiO_2 contents measured by EPMA, B concentrations of unknowns were calculated relative to the $^{11}B^+/^{28}Si^{2+}$ ion yields from the standard used to bracket samples (*26*, *79*).

A B isotope dataset which included duplicate analysis on some grains analyzed by SIMS was collected using an LA-MC-ICP-MS. Analyses were made using a New Wave UP-193-FX ATL excimer laser attached to a Thermo Fisher Scientific Neptune Plus MC-ICP-MS located at Lamont-Doherty Earth Observatory. Analytical methods followed those in (*82*). Operating conditions for all analyses were 10-Hz repetition rate, 3-μm/s stage speed during the linear scans, and a He flow of 1.45 liters/min. Spot sizes were chosen to produce similar strength of ^{11}B signal across phases with differing B contents: 10 to 80 μm for pyroxene megacrysts, 100 μm for nonmegacrystic pyroxene, and 150 μm for plagioclase. Laser fluence was dependent on spot size and ranged from ~28,000 mJ/cm^2 (150-μm spot) to ~1,000,000 mJ/cm^2 (25-μm spot). Analysis locations were pre-ablated with a spot size ~20 μm larger in diameter before analysis. Calculated $\delta^{11}B$ values were corrected on the basis of spot size following the approach in (*82*); in all cases, this resulted in a change of ≤2.5‰. B concentrations (*c*) were estimated semi-quantitatively using the following relationship, where *I* represents the sample intensity and Ø represents the spot size (*82*)

$$[c]_{\text{sample}} = [c]_{\text{standard}} \times \frac{I_{\text{sample}}}{I_{\text{standard}} \times \left(\frac{\text{Ø}_{\text{sample}}}{\text{Ø}_{\text{standard}}}\right)^2}$$

Boron stable isotope data are presented as $\delta^{11}B$, the ratio of ^{11}B to ^{10}B relative to that of the SRM951 standard as a per mil (‰) value (*83*)

$$\delta^{11}B = \left(\frac{^{11}B/^{10}B_{\text{sample}}}{^{11}B/^{10}B_{\text{SRM951}}} - 1\right) \times 10^3$$

The NIST612 glass standard was used as a bracketing standard between groups of five unknown analyses. The calibration curves used to calculate final $\delta^{11}B$ values were constructed from analyses of the NIST612 standard using different spot sizes. NIST612 and the in-house MVE04-4-3 pyroxene, plagioclase, and amphibole standard were used to monitor and validate measured $\delta^{11}B$ values of unknowns. NIST612 yielded $\delta^{11}B = +0.98 \pm 2.91‰$ (2 SD, $n = 34$), consistent with previously published values of $+0.68 \pm 3.31‰$ (2 SD) (*82*) and $-0.51 \pm 0.52‰$ (*84*), both using the same analytical in situ method. This analysis also agrees with the wet chemistry values ranging from $-1.07 \pm 0.85‰$ (minimum value) (*81*) to $+0.10 \pm 0.40‰$ (maximum value) (*85*). MVE04-4-3 yielded $\delta^{11}B = -13.79 \pm 4.19‰$ (2 SD, $n = 7$), in agreement with the previously published value of $\delta^{11}B = -13.80 \pm 1.71‰$ (*30*).

Results for the three grains analyzed by both SIMS and LA-MC-ICP-MS agree closely between the methods, as has been shown by previous work (*30*, *82*). Analyses of grains 14AD9A_littlepyx and 14AD9A_HAOM1 gave $\delta^{11}B$ values and B concentrations overlapping within 2σ SE uncertainty between the techniques (table S1 and Fig. 3). Grain averages determined for grain 98MA1A differ by 5.5‰, but this may reflect the inherent variability of both B concentrations and $\delta^{11}B$ values measured within some single pyroxene megacryst grains (table S2).

Oxygen isotope analysis and sample preparation

For O isotope analyses, rock and plagioclase megacryst samples were crushed and then sieved. About 2 mg mineral separates of samples with a 14AD- prefix was handpicked by K. Varga; all other samples were handpicked by W.H.P. Plagioclase separates were analyzed for oxygen isotopes by laser fluorination in the Department of Geoscience at the University of Wisconsin-Madison following the methods in (*41*, *86*). Precision of standards and duplicate samples on the days of analyses was ≤±0.18‰ (2σ). Oxygen isotope data are presented as $\delta^{18}O$, the ratio of ^{18}O to ^{16}O relative to that of the VSMOW standard as a per mil (‰) value

$$\delta^{18}O\ (\text{VSMOW}) = \left(\frac{^{18}O/^{16}O_{\text{sample}}}{^{18}O/^{16}O_{\text{VSMOW}}} - 1\right) \times 10^3$$

Neodymium and strontium isotope analysis and sample preparation

For Nd and Sr isotope analyses, plagioclase separates were prepared from rock samples at Rice University. Rock fragments with coarse, glassy plagioclase were selected and washed. The rocks were wrapped in clean paper and coarsely crushed by hand using a clean hammer. Fragments with the largest plagioclase crystals were then wrapped in new paper and crushed to a finer grain size using a pestle or hammer. This fine crushed fraction was sieved using a 1-mm mesh sieve and hand-picked using tweezers under an illuminated binocular microscope. Only plagioclase fragments without overgrown inclusions of other minerals (e.g., pyroxene) were selected. Crystal fragments were rinsed with ethanol after separation. All tools were washed between samples and then cleaned with deionized water and ethanol. Plagioclase separates for each sample were crushed using a CoorsTek 99.5% alumina mortar and pestle (#60374), which was washed, and then cleaned with deionized water and ethanol, between samples. Approximately 500 mg to 1 g of crushed plagioclase was prepared from each sample.

Neodymium and Sr isotope analyses were performed in the RIGL at Washington State University. Both Nd and Sr isotope compositions were determined on the same sample aliquots. For each aliquot, approximately 0.25 g of finely ground whole-rock powder was dissolved in high-pressure, steel-jacketed Teflon bombs at 150°C for 7 days using a ~10:1 mixture of concentrated HF and HNO_3. After dissolution and conversion to chloride form using H_3BO_3, sample solutions were spiked with a mixed ^{149}Sm-^{150}Nd tracer, heated in sealed Savillex capsules to facilitate sample-spike equilibration, and passed through initial columns filled with 8 ml of Dowex AG50W-X8 cation exchange resin. This column isolates Sr from the light rare earth elements, Sm and Nd. Sr was subsequently purified using microcolumns with 0.18-ml Eichrom Sr spec resin. Sm and Nd were isolated using columns with 1.7-ml Eichrom Ln Spec resin.

The isotopic compositions of Sr and spiked Sm and Nd solutions were determined using RIGL's Thermo Fisher Scientific Neptune Plus MC-ICP-MS. Samarium and Nd concentrations and Sm/Nd ratios were determined by isotope dilution. Rubidium and Sr concentrations and Rb/Sr ratios were determined on aliquots of the initial sample solution before column chemistry on RIGL's Element2 high-resolution ICP-MS. Samarium and Nd isotope ratios were corrected for interference, spike subtraction, and mass bias using an off-line, in-house data reduction program. Strontium isotope compositions were interference- and mass bias–corrected online as part of the Neptune Plus analysis. During the period of the analyses, the Nd

and Sr isotope standards JNdi-1 [$^{143}Nd/^{144}Nd = 0.512115$ (*87*)] and NBS 987 Sr [$^{87}Sr/^{86}Sr = 0.710248$ (*88*)] gave $^{143}Nd/^{144}Nd = 0.512090 \pm 4$ (2 SD) and $^{87}Sr/^{86}Sr = 0.710281 \pm 13$ (2 SD), respectively, in line with long-term RIGL averages. All Nd and Sr isotope values were normalized relative to these published standard values based on these small differences.

Initial Nd and Sr isotope compositions were calculated using the ^{147}Sm decay constant of 6.524×10^{-12} year^{-1} (*89*) and the ^{87}Rb decay constant of 1.3972×10^{-11} year^{-1} (*90*). Epsilon Nd values, the $^{143}Nd/^{144}Nd$ compositions relative to the chondritic uniform reservoir (CHUR) at the same age, were calculated using the model in (*40*) and the Sm-Nd CHUR parameters of $^{147}Sm/^{144}Nd = 0.1960$ and $^{143}Nd/^{144}Nd = 0.512638$ (*91*).

$$\varepsilon_{Nd}(T) = \left(\frac{^{143}Nd/^{144}Nd_{sample}(T)}{^{143}Nd/^{144}Nd_{CHUR}(T)} - 1 \right) \times 10^4$$

Further details on relevant chemical and analytical procedures can be found in (*92*, *93*).

Electron probe microanalysis

Analytical conditions

EPMA was conducted using a JEOL JXA 8530F Hyperprobe in the Rice University, Department of Earth, Environmental and Planetary Sciences. The instrument is equipped with a field emission assisted thermo-ionic (Schottky) emitter, a silicon drift electron dispersive spectrometry detector, and five wavelength dispersive spectrometers (WDS). The WDS EPMA spots used to measure mineral chemistry were placed within ~100 μm of SIMS pits.

Quantitative WDS analysis

The WDS major and minor element analyses for all minerals used conditions of 15-kV acceleration voltage and 20-nA beam current. An x-ray counting time of 20 s was used for each element, with 10 s used for the peak and 5 s each for upper and lower backgrounds. One analytical recipe was used to analyze inosilicates, and another recipe was used to analyze plagioclase. Pyroxene analyses used a focused beam spot (~250 nm), and plagioclase analyses used a 20-μm-diameter beam to avoid loss of Na and K during analysis. Primary and secondary standards of pyroxenes and feldspars were analyzed as unknown and yielded reproducibility errors below 1% and ~2 to 5% for major and minor elements, respectively. Primary natural mineral standards sourced from SPI Supplies were used in calibrations before analysis: SiO_2: olivine (inosilicates) and plagioclase (plagioclase); TiO_2: rutile; Al_2O_3: almandine (inosilicates) and plagioclase (plagioclase); Cr_2O_3: chromite; FeO: olivine; MnO: rhodonite; MgO: olivine; Na_2O: plagioclase; CaO: plagioclase; and K_2O: biotite (inosilicates) and orthoclase (plagioclase). A JEOL Phi-Rho-Z (PRZ) matrix correction was applied to inosilicate analyses, and a ZAF method was used for plagioclase. Mineral formulas presented in tables S3 and S4 were calculated by normalizing to 6 oxygen atoms for pyroxenes and 8 oxygen atoms for plagioclase.

Numerical modeling of magma crystallization

We took two approaches to modeling changes to magma chemistry from assimilation of wallrock and fractional crystallization. The first used the Magma Chamber Simulator software (the version available in March 2023 downloaded from the Magma Chamber Simulator homepage (https://mcs.geol.ucsb.edu/) (*51*, *52*). The Magma Chamber Simulator software calculates phase equilibria by energy minimization using one of several updated versions of the MELTS thermodynamic engine (*94*). We performed calculations using rhyolite-MELTS v.1.2.0 (*95*, *96*), which incorporates an updated fluid mixing model.

Starting bulk compositions of parental magmas were calculated by binary mixing of LTAOC melt and mantle-derived basalt parents, to which 0.5 wt % H_2O and 0.5 wt % CO_2 were added. Water and CO_2 were added to approximate a realistic magma that could be derived from LTAOC that had not completely dehydrated. The "Parent C" high-Al basalt from (*8*) was used as the mantle wedge basalt endmember, and eclogite melt A221K (20 kbar, 1325°C) from (*57*) was used as the LTAOC melt endmember. These compositions were then renormalized to 100.00 wt % to obtain the parental magma starting composition used in the run. Wallrock mass was set in a 1:1 ratio to magma mass. Wallrock bulk compositions were taken from the averages of the mafic, intermediate, and sedimentary/metasedimentary groups in (*56*) and references therein (*97*–*102*). A total of 0.25 wt % H_2O was added to the mafic and intermediate wallrock compositions before normalization, while 1 wt % H_2O was added to the sedimentary/metasedimentary wallrock composition before normalization. Minor elements, MnO, Cr_2O_3, and P_2O_5, were omitted from bulk compositions for modeling. All simulations were performed at 10 kbar.

At any temperature step where >7.5% melt mass fraction was present in the wallrock, the excess melt was added to the parental magma. Runs proceeded until thermal equilibrium between wallrock and magma was reached, but results are plotted only until the magma exceeded 56 wt % SiO_2, as this is more silicic than the observed bulk chemistries for Marcy and Morin anorthosites, gabbroic anorthosites, and gabbros.

The published Marcy and Morin chemical data to which model results are compared in Fig. 5, as well as the xenolith chemical data from which wallrock compositions were taken, are given in table S8. Bulk compositions of Marcy rocks are from (*35*), and the composition of Marcy An_{46} plagioclase is from (*71*). Bulk compositions of Morin rocks are from (*36*, *44*). Previously published oxygen isotope values of Marcy rocks plotted in Fig. 5B are from (*22*).

Following phase equilibria calculations, isotopic evolution of the system was modeled using the Magma Chamber Simulator Trace Element engine. Partition coefficients were set to the default recommended values in the MCS_TraceElement_Isotopes_PC file, which are given in the run summaries for each run and are consistent across runs (table S7).

Wallrock Nd and Sr concentrations and O isotope values were taken from the original references cited in (*56*) and references therein (*97*–*102*). The $^{143}Nd/^{144}Nd$ and $^{87}Sr/^{86}Sr$ ratios of assimilated wallrock were calculated by assuming a 2 Ga age of the rock and calculating its radiogenic isotope composition at 1155 Ma.

For the LTAOC melt, Nd and Sr concentrations used the "hot" AOC melt in (*73*). The MORB from which it was derived originated with a depleted mantle-like radiogenic isotope signature (*38*) 200 Ma before the anorthosite emplacement age. Seawater alteration was assumed to raise the LTAOC $^{87}Sr/^{86}Sr$ ratio but not affect its $^{143}Nd/^{144}Nd$ ratio (*103*). The initial oxygen isotope composition was set to +10‰ (*103*, *104*).

For the mantle-derived basalt, Nd and Sr concentrations were set slightly lower than a modern primitive Cascades tholeiitic basalt (*105*) to account for high degrees of partial melting. A depleted

mantle $^{143}Nd/^{144}Nd$ value was assumed, and a $^{87}Sr/^{86}Sr$ value slightly elevated from a depleted mantle value was assumed to account for subduction-related enrichment. The initial oxygen isotope composition was set to +5.75‰ (*42*).

We also conducted algebraic AFC modeling to compare with the Magma Chamber Simulator results. This approach does not consider the thermodynamic evolution of the system but is a classic way to study the isotopic effects of AFC processes [e.g., (*53*)]. Modeling followed the approach in (*54*), modified to track isotopes by tracking the two masses for the isotope system in question separately and recalculating the isotopic ratio after the AFC calculations. For a given system, masses of the individual isotopes were calculated from the initial isotopic ratio and the element's concentration (parts per million by mass). As a simplifying assumption, bulk partition coefficients were set at constant values for the duration of the AFC process and were estimated from the values in (*106*) assuming 50% clinopyroxene, 25% garnet, and 25% plagioclase as crystallization products. These proportions are similar to those produced by the Magma Chamber Simulator simulations (table S9). A bulk Nd partition coefficient was calculated to be 0.16 from values of 0.21 for clinopyroxene, 0.087 for garnet, and 0.16 for plagioclase. A bulk Sr partition coefficient was calculated to be 0.53 from values of 0.067 for clinopyroxene, 0.0011 for garnet, and 2 for plagioclase. Oxygen partitioning was assumed to be equal between melt and cumulus phases ($D = 1$). These bulk partition coefficients produce an isotopic evolution trend of the magma extremely similar to that of the Magma Chamber Simulator runs (fig. S4).

Figure 3 data sources

Literature data for $\delta^{11}B$ values and B concentrations of serpentinites, altered oceanic crust, slab-top silicic sediments, arc magmas, seawater, the depleted mantle and MORB, and the bulk continental crust are from the following references: (*25*, *26*, *30*, *33*, *65*, *104*, *107*–*127*).

Supplementary Materials

The PDF file includes:

Figs. S1 to S6
Tables S1 to S6
Legends for tables S7 to S15
References

Other Supplementary Material for this manuscript includes the following:

Tables S7 to S15

REFERENCES AND NOTES

1. L. D. Ashwal, *Anorthosites* (Springer-Verlag, 1993), p. 422.
2. P. Sotiriou, A. Polat, Petrogenesis of anorthosites throughout Earth history. *Precambrian Res.* **384**, 106936 (2023).
3. C. Rey-Moral, T. Mochales, E. Merino Martínez, J. L. García Lobón, M. T. López Bahut, R. Martín-Banda, M. C. Feria, D. Ballesteros, A. Machadinho, D. Alves, Recording the largest gabbro-anorthositic complex worldwide: The Kunene Complex (KC), SW Angola. *Precambrian Res.* **379**, 106790 (2022).
4. L. D. Ashwal, G. M. Bybee, Crustal evolution and the temporality of anorthosites. *Earth Sci. Rev.* **173**, 307–330 (2017).
5. C. O'Neill, M. Brown, B. Schaefer, J. A. Gazi, Earth's anomalous middle-age magmatism driven by plate slowdown. *Sci. Rep.* **12**, 10460 (2022).
6. N. M. W. Roberts, J. Salminen, Å. Johansson, R. N. Mitchell, R. M. Palin, K. C. Condie, C. J. Spencer, On the enigmatic mid-Proterozoic: Single-lid versus plate tectonics. *Earth Planet. Sci. Lett.* **594**, 117749 (2022).
7. B. Charlier, J.-C. Duchesne, J. Vander Auwera, J.-Y. Storme, R. Maquil, J. Longhi, Polybaric fractional crystallization of high-alumina basalt parental magmas in the Egersund–Ogna massif-type Anorthosite (Rogaland, SW Norway) constrained by plagioclase and high-alumina orthopyroxene Megacrysts. *J. Petrol.* **51**, 2515–2546 (2010).
8. R. Fred, J. S. Heinonen, A. Heinonen, W. A. Bohrson, Thermodynamic constraints on the petrogenesis of massif-type anorthosites and their parental magmas. *Lithos* **422-423**, 106751 (2022).
9. G. M. Bybee, L. D. Ashwal, S. B. Shirey, M. Horan, T. Mock, T. B. Andersen, Pyroxene megacrysts in Proterozoic anorthosites: Implications for tectonic setting, magma source and magmatic processes at the Moho. *Earth Planet. Sci. Lett.* **389**, 74–85 (2014).
10. J. W. Valley, J. R. O'Neil, Oxygen isotope evidence for shallow emplacement of Adirondack anorthosite. *Nature* **300**, 497–500 (1982).
11. A. Heinonen, H. Kivisaari, R. M. Michallik, High-aluminum orthopyroxene megacrysts (HAOM) in the Ahvenisto complex, SE Finland, and the polybaric crystallization of massif-type anorthosites. *Contrib. Mineral. Petrol.* **175**, 10 (2020).
12. A. B. Mukherjee, S. Das, D. Sen, B. Bhattacharya, Buoyant rise of anorthosite from a layered basic complex triggered by Rayleigh-Taylor instability: Insights from a numerical modeling study. *Am. Mineral.* **10**, 437–446 (2020).
13. G. M. Bybee, B. Hayes, T. M. Owen-Smith, J. Lehmann, L. D. Ashwal, A. M. Brower, C. M. Hill, F. Corfu, M. Manga, Proterozoic massif-type anorthosites as the archetypes of long-lived (≥100 Myr) magmatic systems—New evidence from the Kunene Anorthosite Complex (Angola). *Precambrian Res.* **332**, 105393 (2019).
14. H. Schiellerup, D. D. Lambert, T. Prestvik, B. Robins, J. S. McBride, R. B. Larsen, Re–Os isotopic evidence for a lower crustal origin of massif-type anorthosites. *Nature* **405**, 781–784 (2000).
15. J. Longhi, A mantle or mafic crustal source for Proterozoic anorthosites? *Lithos* **83**, 183–198 (2005).
16. J. M. McLelland, B. W. Selleck, M. A. Hamilton, M. E. Bickford, Late-to post-tectonic setting of some major Proterozoic anorthosite–mangerite–charnockite–granite (AMCG) suites. *Can. Mineral.* **48**, 729–750 (2010).
17. T. Slagstad, I. H. C. Henderson, N. M. W. Roberts, E. V. Kulakov, M. Ganerød, C. L. Kirkland, B. Dalslåen, R. A. Creaser, N. Coint, Anorthosite formation and emplacement coupled with differential tectonic exhumation of ultrahigh-temperature rocks in a Sveconorwegian continental back-arc setting. *Precambrian Res.* **376**, 106695 (2022).
18. W. H. Peck, J. W. Valley, Large crustal input to high $\delta^{18}O$ anorthosite massifs of the southern Grenville Province: New evidence from the Morin Complex, Quebec. *Contrib. Mineral. Petrol.* **139**, 402–417 (2000).
19. J. M. McLelland, M. E. Bickford, B. M. Hill, C. C. Clechenko, J. W. Valley, M. A. Hamilton, Direct dating of Adirondack massif anorthosite by U-Pb SHRIMP analysis of igneous zircon: Implications for AMCG complexes. *GSA Bulletin* **116**, 1299–1317 (2004).
20. W. H. Peck, B. W. Selleck, S. P. Regan, G. E. Howard, O. O. Kozel, In-situ dating of metamorphism in Adirondack anorthosite. *Am. Mineral.* **103**, 1523–1529 (2018).
21. W. H. Peck, M. P. Quinan, New age constraints on magmatism and metamorphism in the Morin terrane (Grenville Province, Quebec). *Can. J. Earth Sci.* **59**, 232–242 (2022).
22. J. Morrison, J. W. Valley, Contamination of the Marcy Anorthosite Massif, Adirondack Mountains, NY: Petrologic and isotopic evidence. *Contrib. Mineral. Petrol.* **98**, 97–108 (1988).
23. H. W. Jaffe, J. C. Schumacher, Garnet and plagioclase exsolved from aluminum-rich orthopyroxene in the Marcy anorthosite, northeastern Adirondacks, New York. *Can. Mineral.* **23**, 457–478 (1985).
24. H. R. Marschall, "Boron isotopes in the ocean floor realm and the mantle" in *Boron Isotopes–The Fifth Element. Advances in Isotope Geochemistry*, H. R. Marschall, G. L. Foster, Eds. (Springer, 2018), pp. 189–215.
25. C. Martin, K. E. Flores, A. Vitale-Brovarone, S. Angiboust, G. E. Harlow, Deep mantle serpentinization in subduction zones: Insight from in situ B isotopes in slab and mantle wedge serpentinites. *Chem. Geol.* **545**, 119637 (2020).
26. H. R. Marschall, V. D. Wanless, N. Shimizu, P. A. E. Pogge von Strandmann, T. Elliott, B. D. Monteleone, The boron and lithium isotopic composition of mid-ocean ridge basalts and the mantle. *Geochim. Cosmochim. Acta* **207**, 102–138 (2017).
27. S. M. Peacock, R. L. Hervig, Boron isotopic composition of subduction-zone metamorphic rocks. *Chem. Geol.* **160**, 281–290 (1999).
28. H. R. Marschall, R. Altherr, L. Rüpke, Squeezing out the slab—Modelling the release of Li, Be and B during progressive high-pressure metamorphism. *Chem. Geol.* **239**, 323–335 (2007).
29. L. D. Benton, J. G. Ryan, F. Tera, Boron isotope systematics of slab fluids as inferred from a serpentine seamount, Mariana forearc. *Earth Planet. Sci. Lett.* **187**, 273–282 (2001).
30. C. Martin, K. E. Flores, G. E. Harlow, Boron isotopic discrimination for subduction-related serpentinites. *Geology* **44**, 899–902 (2016).
31. J. C. M. De Hoog, E. Clarke, K. Hattori, Mantle wedge olivine modifies slab-derived fluids: Implications for fluid transport from slab to arc magma source. *Geology* **51**, 663–667 (2023).
32. C. Martin, K. E. Flores, G. E. Harlow, S. Angiboust, F. Hodel, G. L. Guice, The B isotopic signature of serpentine from obducted ophiolites: Mixing of fluids and tectonic implications. *Lithos* **456-457**, 107275 (2023).
33. E. F. Rose, N. Shimizu, G. D. Layne, T. L. Grove, Melt production beneath Mt. Shasta from Boron Data in primitive melt inclusions. *Science* **293**, 281–283 (2001).

34. J. M. McLelland, L. Ashwal, L. Moore, Composition and petrogenesis of oxide-, apatite-rich gabbronorites associated with Proterozoic anorthosite massifs: Examples from the Adirondack Mountains, New York. *Contrib. Mineral. Petrol.* **116**, 225–238 (1994).
35. K. E. Seifert, R. F. Dymek, P. R. Whitney, L. A. Haskin, Geochemistry of massif anorthosite and associated rocks, Adirondack Mountains, New York. *Geosphere* **6**, 855–899 (2010).
36. E. R. Pogue, "Petrogenesis of the Morin anorthosite: Grenville Province, Quebec," thesis, Washington Univ., St. Louis, MO (1999).
37. S. R. Bohlen, E. J. Essene, Igneous pyroxenes from metamorphosed anorthosite massifs. *Contrib. Mineral. Petrol.* **65**, 433–442 (1978).
38. L. D. Ashwal, J. L. Wooden, Sr and Nd isotope geochronology, geologic history, and origin of the Adirondack Anorthosite. *Geochim. Cosmochim. Acta* **47**, 1875–1885 (1983).
39. W. H. Peck, J. W. Valley, L. Corriveau, A. Davidson, J. McLelland, D. A. Farber, Oxygen-isotope constraints on terrane boundaries and origin of 1.18–1.13 Ga granitoids in the southern Grenville province. *Memoirs* **197**, 163–182 (2004).
40. D. J. DePaolo, Neodymium isotopes in the Colorado Front Range and crust–mantle evolution in the Proterozoic. *Nature* **291**, 193–196 (1981).
41. W. H. Peck, C. C. Clechenko, M. A. Hamilton, J. W. Valley, Oxygen isotopes in the Grenville and Nain AMCG suites: Regional aspects of the crustal component in massif anorthosites. *Can. Mineral.* **48**, 763–786 (2010).
42. I. N. Bindeman, V. V. Ponomareva, J. C. Bailey, J. W. Valley, Volcanic arc of Kamchatka: A province with high-$\delta^{18}O$ magma sources and large-scale $^{18}O/^{16}O$ depletion of the upper crust. *Geochim. Cosmochim. Acta* **68**, 841–865 (2004).
43. R. T. Gregory, H. P. Taylor Jr., An oxygen isotope profile in a section of Cretaceous Oceanic Crust, Samail Ophiolite, Oman: Evidence for $\delta^{18}O$ buffering of the oceans by deep (>5 km) seawater-hydrothermal circulation at mid-ocean ridges. *J. Geophys. Res.* **86**, 2737–2755 (1981).
44. V. S. Papezik, Geochemistry of some Canadian anorthosites. *Geochim. Cosmochim. Acta* **29**, 678–709 (1965).
45. K. E. Seifert, A. F. Voigt, M. F. Smith, W. A. Stensland, Rare earths in the Marcy and Morin anorthosite complexes. *Can. J. Earth Sci.* **14**, 1033–1045 (1977).
46. D. Demaiffe, D. Weis, J. Michot, J. C. Duchesne, Isotopic constraints on the genesis of the Rogaland anorthositic suite (southwest Norway). *Chem. Geol.* **57**, 167–179 (1986).
47. D. J. Geist, C. D. Frost, A. Kolker, Sr and Nd isotopic constraints on the origin of the Laramie Anorthosite Complex Wyoming. *Am. Mineral.* **75**, 13–20 (1990).
48. R. F. Emslie, M. A. Hamilton, R. J. Thériault, Petrogenesis of a mid-Proterozoic anorthosite-mangerite-charnockite-granite (AMCG) complex: Isotopic and chemical evidence from the Nain Plutonic Suite. *J. Geol.* **102**, 539–558 (1994).
49. P. Gleißner, K. Drüppel, R. L. Romer, The role of crustal contamination in massif-type anorthosites, new evidence from Sr-Nd-Pb isotopic composition of the Kunene Intrusive Complex, NW Namibia. *Precambrian Res.* **185**, 18–36 (2011).
50. A. Heinonen, T. Andersen, O. T. Rämö, M. J. Whitehouse, The source of Proterozoic anorthosite and rapakivi granite magmatism: Evidence from combined in situ Hf–O isotopes of zircon in the Ahvenisto complex, southeastern Finland. *J. Geol. Soc. London* **172**, 103–112 (2015).
51. W. A. Bohrson, F. J. Spera, J. S. Heinonen, G. A. Brown, M. A. Scruggs, J. V. Adams, M. K. Takach, G. Zeff, E. Suikkanen, Diagnosing open-system magmatic processes using the Magma Chamber Simulator (MCS): Part I—Major elements and phase equilibria. *Contrib. Mineral. Petrol.* **175**, 104 (2020).
52. J. S. Heinonen, W. A. Bohrson, F. J. Spera, G. A. Brown, M. A. Scruggs, J. V. Adams, Diagnosing open-system magmatic processes using the Magma Chamber Simulator (MCS): Part II—Trace elements and isotopes. *Contrib. Mineral. Petrol.* **175**, doi: 10.1007/s00410-020-01718-9 (2020).
53. D. J. DePaolo, Trace element and isotopic effects of combined wallrock assimilation and fractional crystallization. *Earth Planet. Sci. Lett.* **53**, 189–202 (1981).
54. C.-T. A. Lee, T. C. Lee, C.-T. Wu, Modeling the compositional evolution of recharging, evacuating, and fractionating (REFC) magma chambers: Implications for differentiation of arc magmas. *Geochim. et Cosmochim. Acta* **143**, 8–22 (2014).
55. G. A. Snyder, L. A. Taylor, G. Crozaz, A. N. Halliday, B. L. Beard, V. N. Sobolev, N. V. Sobolev, The origins of Yakutian eclogite xenoliths. *J. Petrol.* **38**, 85–113 (1997).
56. P. D. Kempton, R. S. Harmon, Oxygen isotope evidence for large-scale hybridization of the lower crust during magmatic underplating. *Geochim. et Cosmochim. Acta* **56**, 971–986 (1992).
57. M. Pertermann, M. M. Hirschmann, Anhydrous partial melting experiments on MORB-like eclogite: Phase relations, phase compositions and mineral–melt partitioning of major elements at 2–3 GPa. *J. Petrol.* **44**, 2173–2201 (2003).
58. C. Kuebler, A. Simonetti, S. S. Simonetti, R. F. Martin, Boron isotope compositions establish the origin of marble from metamorphic complexes: Québec, New York, and Sri Lanka. *Am. Mineral.* **107**, 15–30 (2022).
59. P. R. Phelps, C.-T. A. Lee, Extreme lithium isotope fractionation in quartz from the Stewart pegmatite. *Geochim. et Cosmochim. Acta* **336**, 208–218 (2022).
60. J. J. Ague, J. A. Axler, Interface coupled dissolution-reprecipitation in garnet from subducted granulites and ultrahigh-pressure rocks revealed by phosphorous, sodium, and titanium zonation. *Am. Mineral.* **101**, 1696–1699 (2016).
61. D. S. Keller, J. J. Ague, High-pressure granulite facies metamorphism (~1.8 GPa) revealed in silica-undersaturated garnet-spinel-corundum gneiss, Central Maine Terrane, Connecticut, U.S.A. *Am. Mineral.* **103**, 1851–1868 (2018).
62. R. L. Hervig, G. M. Moore, L. B. Williams, S. M. Peacock, J. R. Holloway, K. Roggensack, Isotopic and elemental partitioning of boron between hydrous fluid and silicate melt. *Am. Mineral.* **87**, 769–774 (2002).
63. U. Hålenius, H. Skogby, M. Edén, S. Nazzareni, P. Kristiansson, J. Resmark, Coordination of boron in nominally boron-free rock forming silicates: Evidence for incorporation of BO_3 groups in clinopyroxene. *Geochim. et Cosmochim. Acta* **74**, 5672–5679 (2010).
64. B. Wunder, J. Stefanski, R. Wirth, M. Gottschalk, Al-B substitution in the system albite ($NaAlSi_3O_8$)–reedmergnerite ($NaBSi_3O_8$). *Eur. J. Mineral.* **25**, 499–508 (2013).
65. J. C. M. De Hoog, I. P. Savov, "Boron isotopes as a tracer of subduction zone processes" in *Boron Isotopes–The Fifth Element. Advances in Isotope Geochemistry*, H. R. Marschall, G. L. Foster, Eds. (Springer, 2018), pp. 217–247.
66. Z. Huang, C. Yuan, X. Long, Y. Zhang, X. Ma, J. Soldner, L. Du, C. Shu, The cause for Nuna breakup in the early to middle mesoproterozoic. *Precambrian Res.* **362**, 106287 (2022).
67. P. A. Brandl, M. Regelous, C. Beier, K. M. Haase, High mantle temperatures following rifting caused by continental insulation. *Nat. Geosci.* **6**, 391–394 (2013).
68. J. M. McLelland, J. Chiarenzelli, Isotopic constraints on emplacement age of anorthositic rocks of the Marcy massif, Adirondack Mts., New York. *J. Geol.* **98**, 19–41 (1989).
69. W. H. Peck, Reconnaissance geochronology and geochemistry of the Mont-Tremblant gneiss of the Morin terrane, Grenville Province Québec. *Geosphere* **8**, 1356–1365 (2012).
70. W. H. Peck, B. W. Selleck, M. S. Wong, J. R. Chiarenzelli, K. S. Harpp, K. Hollocher, J. S. Lackey, J. Catalano, S. P. Regan, A. Stocker, Orogenic to postorogenic (1.20–1.15 Ga) magmatism in the Adirondack Lowlands and Frontenac terrane, southern Grenville Province, USA and Canada. *Geosphere* **9**, 1637–1663 (2013).
71. L. D. Ashwal, Mineralogy of mafic and Fe–Ti oxide-rich differentiates of the Marcy anorthosite massif, Adirondacks New York. *Am. Mineral.* **67**, 14–27 (1982).
72. I. N. Bindeman, J. M. Eiler, G. M. Yogodzinski, Y. Tatsumi, C. R. Stern, T. L. Grove, M. Portnyagin, K. Hoernle, L. V. Danyushevsky, Oxygen isotope evidence for slab melting in modern and ancient subduction zones. *Earth Planet. Sci. Lett.* **235**, 480–496 (2005).
73. S. J. Turner, C. H. Langmuir, Sediment and ocean crust both melt at subduction zones. *Earth Planet. Sci. Lett.* **584**, 117424 (2022).
74. C. Herzberg, K. Condie, J. Korenaga, Thermal history of the Earth and its petrological expression. *Earth Planet. Sci. Lett.* **292**, 79–88 (2010).
75. R. M. Palin, M. Santosh, W. Cao, S.-S. Li, D. Hernández-Uribe, A. Parsons, Secular change and the onset of plate tectonics on Earth. *Earth Sci. Rev.* **207**, 103172 (2020).
76. C. J. Hawkesworth, P. A. Cawood, B. Dhuime, The evolution of the continental crust and the onset of plate tectonics. *Front. Earth Sci.* **8**, 326 (2020).
77. W. H. Peck, "Oxygen isotope studies of Grenville metamorphism and magmatism," thesis, Univ. of Wisconsin, Madison, WI (2000).
78. W. H. Peck, B. W. Selleck, J. W. Valley, M. J. Spicuzza, A. T. Taylor, Emplacement and metamorphism of the Marcy anorthosite: New constraints from geochronology and oxygen isotopes. *Geol. Soc. Am. Abstr. Programs* **49**, doi: 10.1130/abs/2017AM-299676 (2017).
79. H. R. Marschall, B. D. Monteleone, Boron isotope analysis of silicate glass with very low boron concentrations by secondary ion mass spectrometry. *Geostand. Geoanal. Res.* **39**, 31–46 (2014).
80. M. Chaussidon, F. Robert, D. Mangin, P. Hanon, E. F. Rose, Analytical procedures for the measurement of boron isotope compositions by ion microprobe in meteorites and mantle rocks. *Geostand. Newsl.* **21**, 7–17 (1997).
81. S. Kasemann, A. Meixner, A. Rocholl, T. Vennemann, M. Rosner, A. K. Schmitt, M. Wiedenbeck, Boron and oxygen isotope composition of certified reference materials NIST SRM 610/612 and reference materials JB-2 and JR-2. *Geostand. Newsl.* **25**, 405–416 (2001).
82. C. Martin, E. Ponzereva, G. Harlow, In situ lithium and boron isotope determinations in mica, pyroxene, and serpentine by LA-MC-ICP-MS. *Chem. Geol.* **412**, 107–116 (2015).
83. E. J. Catanzaro, *Boric Acid: Isotopic and Assay Standard Reference Materials* (National Bureau of Standards, Institute for Materials Research, 1970).
84. J.-I. Kimura, Q. Chang, T. Ishikawa, T. Tsujimori, Influence of laser parameters on isotope fractionation and optimisation of lithium and boron isotope ratio measurements using laser ablation-multiple Faraday collector-inductively coupled plasma mass spectrometry. *J. Anal. At. Spectrom* **31**, 2305–2320 (2016).
85. K. P. Jochum, S. A. Wilson, W. Abouchami, M. Amini, J. Chmeleff, A. Eisenhauer, E. Hegner, L. M. Iaccheri, B. Kieffer, J. Krause, W. F. McDonough, R. Mertz-Kraus, I. Raczek, R. L. Rudnick, D. Scholz, G. Steinhoefel, B. Stoll, A. Stracke, S. Tonarini, D. Weis, U. Weis, J. D. Woodhead, GSD-1G and MPI-DING reference glasses for in situ and bulk isotopic determination. *Geostand. Geoanal. Res.* **35**, 193–226 (2011).

86. J. W. Valley, N. Kitchen, M. J. Kohn, C. R. Niendorf, M. J. Spicuzza, UWG-2, a garnet standard for oxygen isotope ratios: Strategies for high precision and accuracy with laser heating. *Geochim. et Cosmochim. Acta* **59**, 5223–5231 (1995).
87. T. Tanaka, S. Togashi, H. Kamioka, H. Amakawa, H. Kagami, T. Hamamoto, M. Yuhara, Y. Orihashi, S. Yoneda, H. Shimizu, T. Kunimaru, K. Takahashi, T. Yanagi, T. Nakano, H. Fujimaki, R. Shinjo, Y. Asahara, M. Tanimizu, C. Dragusanu, JNdi-1: A neodymium isotopic reference in consistency with LaJolla neodymium. *Chem. Geol.* **168**, 279–281 (2000).
88. D. Weis, B. Kieffer, C. Maerschalk, J. Barling, J. de Jong, G. A. Williams, D. Hanano, W. Pretorius, N. Mattielli, J. S. Scoates, A. Goolaerts, R. M. Friedman, J. B. Mahoney, High-precision isotopic characterization of USGS reference materials by TIMS and MC-ICP-MS. *Geochem. Geophys. Geosyst.* **7**, Q08006 (2006).
89. I. M. Villa, N. E. Holden, A. Possolo, R. B. Ickert, D. B. Hibbert, P. R. Renne, IUPAC-IUGS recommendation on the half-lives of ^{147}Sm and ^{146}Sm. *Geochim. et Cosmochim. Acta* **285**, 70–77 (2020).
90. I. M. Villa, P. De Bièvre, N. E. Holden, P. R. Renne, IUPAC-IUGS recommendation on the half life of ^{87}Rb. *Geochim. et Cosmochim. Acta* **164**, 382–385 (2015).
91. A. Bouvier, J. D. Vervoort, P. J. Patchett, The Lu–Hf and Sm–Nd isotopic composition of CHUR: Constraints from unequilibrated chondrites and implications for the bulk composition of terrestrial planets. *Earth Planet. Sci. Lett.* **273**, 48–57 (2008).
92. R. M. Gaschnig, J. D. Vervoort, R. S. Lewis, B. Tikoff, Isotopic evolution of the Idaho batholith and challis intrusive province northern US Cordillera. *J. Petrol.* **52**, 2397–2429 (2011).
93. T. A. Johnson, J. D. Vervoort, M. J. Ramsey, J. N. Aleinikoff, S. Southworth, Constraints on the timing and duration of orogenic events by combined Lu–Hf and Sm–Nd geochronology: An example from the Grenville orogeny. *Earth Planet. Sci. Lett.* **501**, 152–164 (2018).
94. M. S. Ghiorso, R. O. Sack, Chemical mass transfer in magmatic processes IV. A revised and internally consistent thermodynamic model for the interpolation and extrapolation of liquid-solid equilibria in magmatic systems at elevated temperatures and pressures. *Contrib. Mineral. Petrol.* **119**, 197–212 (1995).
95. G. A. R. Gualda, M. S. Ghiorso, R. V. Lemons, T. L. Carley, Rhyolite-MELTS: A modified calibration of MELTS optimized for silica-rich, Fluid-bearing Magmatic Systems. *J. Petrol.* **53**, 875–890 (2012).
96. M. S. Ghiorso, G. A. R. Gualda, An H_2O–CO_2 mixed fluid saturation model compatible with rhyolite-MELTS. *Contrib. Mineral. Petrol.* **169**, 53 (2015).
97. R. L. Rudnick, W. F. McDonough, M. T. McCulloch, S. R. Taylor, Lower crustal xenoliths from Queensland, Australia: Evidence for deep crustal assimilation and fractionation of continental basalts. *Geochim. Cosmochim. Acta* **50**, 1099–1115 (1986).
98. H.-G. Stosch, G. W. Lugmair, H. A. Seck, Geochemistry of granulite-facies lower crustal xenoliths: Implications for the geological history of the lower continental crust below the Eifel, West Germany. *Geol. Soc. Spec. Publ.* **24**, 309–317 (1986).
99. R. L. Rudnick, S. R. Taylor, The composition and petrogenesis of the lower crust: A xenolith study. *J. Geophys. Res.* **92**, 13981–14005 (1987).
100. H. Downes, C. Dupuy, A. F. Leyreloup, Crustal evolution of the Hercynian belt of Western Europe: Evidence from lower-crustal granulitic xenoliths (French Massif Central). *Chem. Geol.* **83**, 209–231 (1990).
101. G. Loock, H.-G. Stosch, H. A. Seck, Granulite facies lower crustal xenoliths from the Eifel, West Germany: Petrological and geochemical aspects. *Contrib. Mineral. Petrol.* **105**, 25–41 (1990).
102. H. Downes, P. D. Kempton, D. Briot, R. S. Harmon, A. F. Leyreloup, Pb and O isotope systematics in granulite facies xenoliths, French Massif Central: Implications for crustal processes. *Earth Planet. Sci. Lett.* **102**, 342–357 (1991).
103. M. T. McCulloch, R. T. Gregory, G. J. Wasserburg, H. P. Taylor Jr., Sm-Nd, Rb-Sr, and $^{18}O/^{16}O$ isotopic systematics in an oceanic crustal section: Evidence from the Samail ophiolite. *J. Geophys. Res.* **86**, 2721–2735 (1981).
104. H. J. Smith, A. J. Spivack, H. Staudigel, S. R. Hart, The boron isotopic composition of altered oceanic crust. *Chem. Geol.* **126**, 119–135 (1995).
105. M. W. Schmidt, O. Jagoutz, The global systematics of primitive arc melts. *Geochem. Geophys. Geosyst.* **18**, 2817–2854 (2017).
106. D. McKenzie, R. K. O'Nions, Partial melt distributions from inversion of rare Earth element concentrations. *J. Petrol.* **32**, 1021–1091 (1991).
107. C. Boschi, A. Dini, G. L. Früh-Green, D. S. Kelley, Isotopic and element exchange during serpentinization and metasomatism at the Atlantis Massif (MAR 30°N): Insights from B and Sr isotope data. *Geochim. Cosmochim. Acta* **72**, 1801–1823 (2008).
108. F. Vils, S. Tonarini, A. Kalt, H.-M. Seitz, Boron, lithium and strontium isotopes as tracers of seawater-serpentinite interaction at Mid-Atlantic ridge, ODP Leg 209. *Earth Planet. Sci. Lett.* **286**, 414–425 (2009).
109. M. Scambelluri, S. Tonarini, Boron isotope evidence for shallow fluid transfer across subduction zones by serpentinized mantle. *Geology* **40**, 907–910 (2012).
110. C. Boschi, E. Bonatti, M. Ligi, D. Brunelli, A. Cipriani, L. Dallai, M. D'Orazio, G. L. Früh-Green, S. Tonarini, J. D. Barnes, R. M. Bedini, Serpentinization of mantle peridotites along an uplifted lithospheric section, Mid Atlantic Ridge at 11° N. *Lithos* **178**, 3–23 (2013).
111. J. Harvey, C. J. Garrido, I. Savov, S. Agostini, J. A. Padrón-Navarta, C. Marchesi, V. López Sánchez-Vizcaíno, M. T. Gómez-Pugnaire, ^{11}B-rich fluids in subduction zones: The role of antigorite dehydration in subducting slabs and boron isotope heterogeneity in the mantle. *Chem. Geol.* **376**, 20–30 (2014).
112. J. Harvey, I. P. Savov, S. Agostini, R. A. Cliff, R. Walshaw, Si-metasomatism in serpentinized peridotite: The effects of talc-alteration on strontium and boron isotopes in abyssal serpentinites from Hole 1268a, ODP Leg 209. *Geochim. Cosmochim. Acta* **126**, 30–48 (2014).
113. E. Cannaò, S. Agostini, M. Scambelluri, S. Tonarini, M. Godard, B, Sr and Pb isotope geochemistry of high-pressure Alpine metaperidotites monitors fluid-mediated element recycling during serpentinite dehydration in subduction mélange (Cima di Gagnone, Swiss Central Alps). *Geochim. Cosmochim. Acta* **163**, 80–100 (2015).
114. E. Cannaò, M. Scambelluri, S. Agostini, S. Tonarini, M. Godard, Linking serpentinite geochemistry with tectonic evolution at the subduction plate-interface: The Voltri Massif case study (Ligurian Western Alps, Italy). *Geochim. Cosmochim. Acta* **190**, 115–133 (2016).
115. K. Yamaoka, T. Ishikawa, O. Matsubaya, D. Ishiyama, K. Nagaishi, Y. Hiroyasu, H. Chiba, H. Kawahata, Boron and oxygen isotope systematics for a complete section of oceanic crustal rocks in the Oman ophiolite. *Geochim. Cosmochim. Acta* **84**, 543–559 (2012).
116. K. Yamaoka, S. Matsukura, T. Ishikawa, H. Kawahata, Boron isotope systematics of a fossil hydrothermal system from the Troodos ophiolite, Cyprus: Water-rock interactions in the oceanic crust and subseafloor ore deposits. *Chem. Geol.* **396**, 61–73 (2015).
117. E. Cannaò, M. Scambelluri, O. Müntener, B. Putlitz, S. Agostini, Inheritance versus subduction-related δ^{11}B signatures of eclogites: Insights from the Voltri Massif (Ligurian Western Alps, Italy). *Chem. Geol.* **615**, 121218 (2023).
118. M. R. Palmer, Boron-isotope systematics of Halmahera arc (Indonesia) lavas: Evidence for involvement of the subducted slab. *Geology* **19**, 215–217 (1991).
119. T. Ishikawa, E. Nakamura, Origin of the slab component in arc lavas from across-arc variation of B and Pb isotopes. *Nature* **370**, 205–208 (1994).
120. T. Ishikawa, F. Tera, T. Nakazawa, Boron isotope and trace element systematics of the three volcanic zones in the Kamchatka arc. *Geochim. Cosmochim. Acta* **65**, 4523–4537 (2001).
121. S. Tonarini, W. P. Leeman, G. Ferrara, Boron isotopic variations in lavas of the Aeolian volcanic arc, South Italy. *J. Volcanol. Geotherm. Res.* **110**, 155–170 (2001).
122. S. Tonarini, W. P. Leeman, P. T. Leat, Subduction erosion of forearc mantle wedge implicated in the genesis of the South Sandwich Island (SSI) arc: Evidence from boron isotope systematics. *Earth Planet. Sci. Lett.* **301**, 275–284 (2011).
123. H.-Y. Li, X. Li, J. G. Ryan, C. Zhang, Y.-G. Xu, Boron isotopes in boninites document rapid changes in slab inputs during subduction initiation. *Nat. Comm.* **13**, 993 (2022).
124. H.-Y. Li, C. Xie, J. G. Ryan, C.-M. Yang, R.-P. Zhao, C. Zhang, Y.-G. Xu, Slab dehydration and magmatism in the Kurile arc as a function of depth: An investigation based on B-Sr-Nd-Hf isotopes. *Chem. Geol.* **621**, 121373 (2023).
125. T. Ishikawa, E. Nakamura, Boron isotope systematics of marine sediments. *Earth Planet. Sci. Lett.* **117**, 567–580 (1993).
126. G. L. Foster, P. A. E. Pogge von Strandmann, J. W. B. Rae, Boron and magnesium isotopic composition of seawater. *Geochem. Geophys. Geosyst.* **11**, Q08015 (2010).
127. P. J. Le Roux, S. B. Shirey, L. Benton, E. H. Hauri, T. D. Mock, In situ, multiple-multiplier, laser ablation ICP-MS measurement of boron isotopic composition (δ^{11}B) at the nanogram level. *Chem. Geol.* **203**, 123–138 (2004).
128. L. D. Ashwal, The temporality of anorthosites. *Can. Mineral.* **48**, 711–728 (2010).
129. K. C. Condie, R. C. Aster, Refinement of the supercontinent cycle with Hf, Nd and Sr isotopes. *Geosci. Front.* **4**, 667–680 (2013).
130. R. P. Tollo, L. Corriveau, J. McLelland, M. J. Bartholomew, Proterozoic tectonic evolution of the Grenville orogen in North America: An introduction. *Geol. Soc. Am. Mem.* **197**, doi: 10.1130/0-8137-1197-5.1 (2004).
131. D. W. Fisher, Y. W. Isachsen, L. V. Rickard, Geologic Map of New York State, consisting of 5 sheets: Niagara, Finger Lakes, Hudson-Mohawk, Adirondack, and Lower Hudson: New York State Museum and Science Service, Map and Chart Series No. 15, scale 1:250,000 (1970).

Acknowledgments: We thank P. Phelps, S. Allen, J. Borchardt, V. Le Roux, D. Viete, L. Kump, X. Chu, A. Haws, J. Ague, and M. Krause for helpful discussions. We thank K. Varga for sample preparation. W.H.P. thanks J. Valley for long-term collaborations on anorthosite geochemistry and for the use of the Stable Isotope Laboratory at the University of Wisconsin and M. Spicuzza for assistance in the lab. Use of the EPMA facility in the Rice University Department of Earth, Environmental and Planetary Sciences is acknowledged. We also thank National Petrographic Service (Rosenberg, TX) for careful preparation of thin sections to specifications. **Funding:** D.S.K. and C.-T.A.L. received support from NASA grant 80NSSC18K0828 and NSF EAR 2139558.

C.M. received support from US National Science Foundation NSF EAR 1951166. **Author contributions:** D.S.K., C.-T.A.L., and W.H.P. designed the study. D.S.K. prepared samples for Nd, Sr, and B isotope analyses and conducted modeling. W.H.P. performed O isotope analyses. J.D.V. oversaw Nd and Sr isotope analyses. D.S.K. and B.D.M. conducted B isotope analyses using SIMS. D.S.K., C.M., and L.B. conducted B isotope analyses using LA-MC-ICP-MS. D.S.K. wrote the first draft of the manuscript, which all authors edited together. **Competing interests:** The authors declare that they have no competing interests. **Data and materials availability:** All data needed to evaluate the conclusions in the paper are present in the paper and/or the Supplementary Materials.

Submitted 8 December 2023
Accepted 9 July 2024
Published 14 August 2024
10.1126/sciadv.adn3976